2009

Charged pion production cross section using 120 GeV/c proton beam on carbon target

Gural Aydin
University of Iowa

Recommended Citation

Aydin, Gural. "Charged pion production cross section using 120 GeV/c proton beam on carbon target." dissertation, University of Iowa, 2009.
http://ir.uiowa.edu/etd/333.

CHARGED PION PRODUCTION CROSS SECTION USING 120 GEV/C PROTON BEAM ON CARBON TARGET

by

Gural Aydin

An Abstract

Of a thesis submitted in partial fulfillment of the
requirements for the Doctor of Philosophy degree
in Physics in
the Graduate College of
The University of Iowa

December 2009

Thesis Supervisor: Professor Yasar Onel

The MIPP (Main Injector Particle Production) Experiment is a fixed target experiment at Fermilab to measure hadronic production for different targets and beam energies. Data were taken in 2005 on targets including aluminum, beryllium, bismuth, carbon, copper, and uranium, a cryogenic hydrogen target, and the NuMI target using six types of beam particles (pion, kaon, and proton of both charges) for the beam energies ranging from 5 GeV/c to 120 GeV/c. We present the charged pion production cross section measurements of 120 GeV/c proton beam on a thin carbon target in terms of final state particle's longitudinal and transverse momenta.

Abstract Approved: ______________________
Thesis Supervisor

____
Title and Department

____
Date

CHARGED PION PRODUCTION CROSS SECTION USING 120 GEV/C PROTON BEAM ON CARBON TARGET

by

Gural Aydin

A thesis submitted in partial fulfillment of the
requirements for the Doctor of
Philosophy degree in Physics in
the Graduate College of
The University of Iowa

December 2009

Thesis Supervisor: Professor Yasar Onel

Graduate College
The University of Iowa
Iowa City, Iowa

CERTIFICATE OF APPROVAL

PH.D. THESIS

This is to certify that the Ph.D. thesis of

Gural Aydin

has been approved by the Examining Committee for the thesis requirement for the Doctor of Philosophy degree in Physics at the December 2009 graduation.

Thesis Committee:

Yasar Onel, Thesis Supervisor

Edwin Norbeck

Robert L. Merlino

Jane M. Nachtman

Tuong Ton-That

to my parents

ACKNOWLEDGMENTS

I thank all members of the MIPP collaboration. Their generous help increased my understanding of physics. I especially thank Holger Meyer, Turgun Nigmanov, Jonhotan Paley, Durga Rajaram, Rajendran Raja for answering my questions and pushing me to work hard. I am grateful to my supervisor Yasar Onel for trusting me and believing that I would be successful. I thank my friend and colleque Yusuf Gunaydin, who was with me in all steps of the graduate study. I thank my parents. They always supported me and gave emotional power when i had hard times in my work.

ABSTRACT

The MIPP (Main Injector Particle Production) Experiment is a fixed target experiment at Fermilab to measure hadronic production for different targets and beam energies. Data were taken in 2005 on targets including aluminum, beryllium, bismuth, carbon, copper, and uranium, a cryogenic hydrogen target, and the NuMI target using six types of beam particles (pion, kaon, and proton of both charges) for the beam energies ranging from 5 GeV/c to 120 GeV/c. We present the charged pion production cross section measurements of 120 GeV/c proton beam on a thin carbon target in terms of final state particle's longitudinal and transverse momenta.

TABLE OF CONTENTS

CHAPTER

LIST OF TABLES

Table

LIST OF FIGURES

Figure

CHAPTER 1
INTRODUCTION

Hadronic production data has a significant impact on neutrino related experiments since neutrinos [21] are obtained from the decay of pions and kaons, which are obtained by allowing the primary proton beam to interact with a target, or muons, which are the decay products of the pions and kaons. The two-body decay processes of pions and kaons are defined as

$$\pi^{\pm} \rightarrow \mu^{\pm} + \nu_{\mu}(\overline{\nu_{\mu}}) \tag{1.1}$$

$$K^{\pm} \rightarrow \mu^{\pm} + \nu_{\mu}(\overline{\nu_{\mu}}) \tag{1.2}$$

Most accelerator neutrino experiments use two detectors to calculate oscillation parameters: a near and far detector. The near detector sees neutrinos as a line source, whereas the far detector sees neutrinos as a point source such as in [2] [3]. So, to predict the neutrino flux at the far detector in the absence of the oscillation, momentum and angle distributions of the neutrinos at the near detector must be known. However, the near detector measures only energy distributions of the neutrinos.

Simulation of the decays of the hadrons gives very accurate results. Therefore, if the hadron production is measured with the same precision, the neutrino beam distribution at the near and far detector could be estimated as well. However, the current experimental data do not cover completely the space in momentum and angle. The Figure 1.1 summarizes the result of the previous experiments. Therefore, hadronic production models [21] like MARS [23] and FLUKA [1], are used to predict the production schema. However, different hadronic models give vastly different results on hadronic production data, so we need to improve experimental data.

In this analysis, we show the production cross section of charged pions with longitudinal momentum between 0.24 GeV/c and 1.0 GeV/c and between 30.0 GeV/c and 60 GeV/c on a thin carbon target with a 120 GeV/c proton beam.

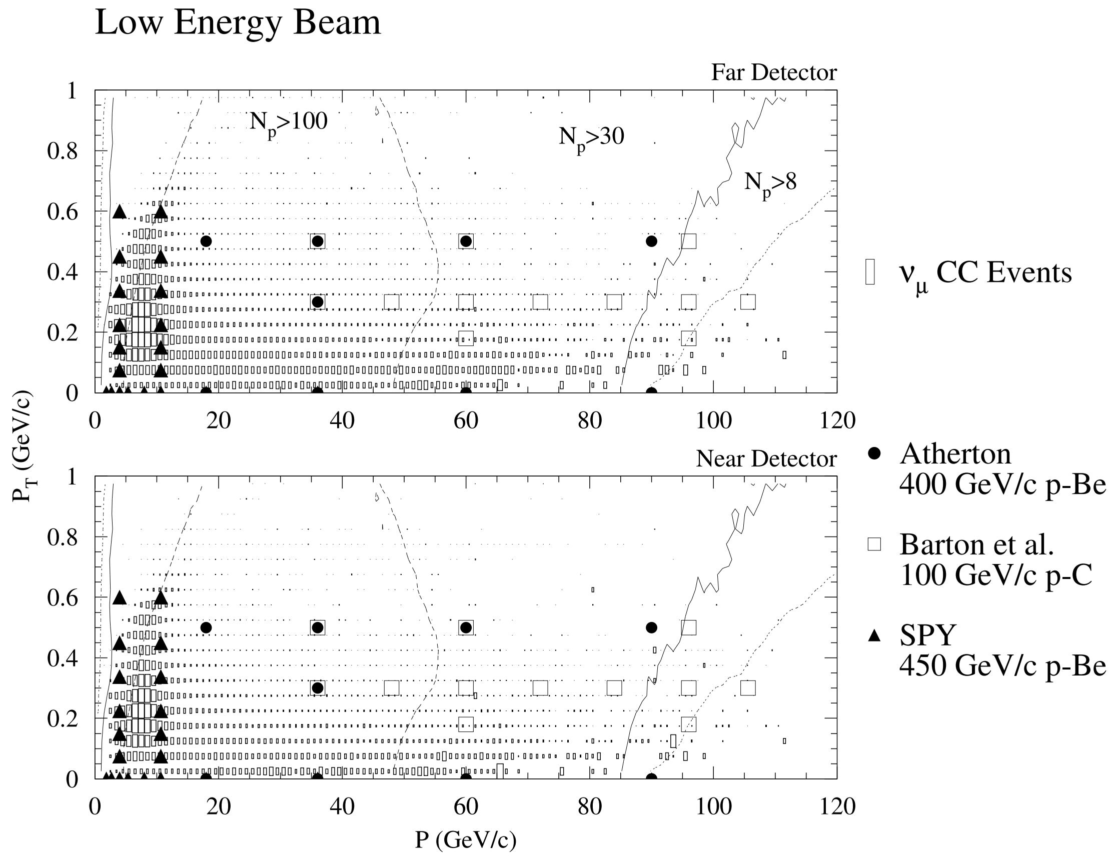

Figure 1.1: P_t vs. P for pions producing neutrinos seen in far (top) and near (bottom) detectors in MINOS with the “Low Energy Beam” horn configuration. Data are taken from [8] [10] [7].

One of the active neutrino experiments is NuMI/MINOS, which uses a 120 GeV/c proton beam on a NuMI target that is made of graphite. So, our analysis obtained from the 120 GeV/c proton beam will provide, at least partially, a better understanding of the neutrino beam flux in the NuMI/MINOS experiment. It will also help to close the gap in hadronic production data and it may contribute to future neutrino factory needs.

1.1 Motivations of the MIPP experiment

The MIPP experiment addresses other physics topics. We briefly describe two of those. More information about the MIPP physics motivations can be read in the MIPP proposal [5].

1.1.1 General Scaling Law of Hadronic Fragmentation

General scaling law of particle fragmentation states that ratio of semi-inclusive cross section to an inclusive cross section is a function of only the missing mass squared (M^2) not a function of the center of mass energy squared (s) or the momentum transfer squared (t).

The law can be formulated

$$\frac{f_{subset}\left(a+b\rightarrow c+X\right)}{f\left(a+b\rightarrow c+X\right)} \equiv \frac{f_{subset}\left(M^2,s,t\right)}{f\left(M^2,s,t\right)} = \beta_{subset}\left(M^2\right) \tag{1.3}$$

The law was tested for t independence using 100 GeV/c beam with $p^{-}p \rightarrow \pi + X$ reaction. The data and the scaling law seemed in a good agreement. Furthermore in reference [24], s independence of the law was confirmed with $pp \rightarrow p + X$ reactions for the beam energy between 200 and 400 GeV/c.

It is not easy to test s independence of the scaling law with the existing data since the data does not have the same experimental apparatus at different energies for the same type of interactions. MIPP(Main Injector Particle Production) experiment is capable of testing the law with 36 reactions, such as $\pi^+ p \rightarrow \pi^+ X$ and $\pi^- p \rightarrow \pi^- X$, at multiple energies using a liquid hydrogen target.

1.1.2 Charged Kaon Mass Measurement

One of the physics motivations of the MIPP is to measure the charged kaon mass using the RICH ring radius. The PDG (Particle Data Group) reports the value of the charged kaon mass as 493.677±0.013 MeV. This value is the weighted mean of six different results. The most recent and precise two measurements are 493.696±0.007 MeV and 493.636±0.011 MeV, which were done by Denisov et al. [11] and Gall et al. [20], respectively. Since the values from different measurements differ significantly, the mass needs to be measured with higher precision using a different method.

In MIPP, the charged kaon mass measurement analysis was performed by N. Graf et al. [18] using the tagged pion, kaon, and proton beams in the momentum range 37 to 63 GeV/c. The mass was measured as 491.3±1.7 MeV within 1.4 σ of the current PDG value. The analysis showed that competitive kaon mass measurements are possible with the RICH technique.

CHAPTER 2
THE MIPP EXPERIMENT

The MIPP (Main Injector Particle Production) Experiment was proposed in 1999 as a fixed target experiment and approved in November, 2001. It was designed as a full acceptance spectrometer. MIPP had engineering runs in summer and winter 2004 and production runs between January 2005 and February 2006. It used 120 GeV/c Main Injector primary proton beams and secondary beams in a momentum range between 5 GeV/c and 90 GeV/c on targets spanning a large range of atomic weight. In this chapter, an overview of the MIPP experimental apparatus will be given.

2.1 Experimental Setup

MIPP is a full acceptance spectrometer located in the Meson Center (MC7) at Fermi National Accelerator Laboratory (FNAL). The design of the detector system allows for particle tracking and identification of charged particles. The spectrometer is shown in Figure 2.1.

The experimental target used in MIPP is placed a few centimeters upstream of the TPC (Time Projection Chamber) front face standing in the Jolly Green Giant (JGG) analyzing magnet. The specifications and installation of the JGG can be found at [**?**]. In the case of our analysis, the z position of the center of the experimental target was at -829.0 cm.

The MIPP coordinate system was a right handed coordinate system with the z axis along the beam direction, the y axis pointing vertically up and the x axis horizontal with respect to the beam direction. The origin of the coordinate system is at the target, although the Geant CAVE volume was centered at approximately 825 cm downstream of the target inside the ROSIE magnet.

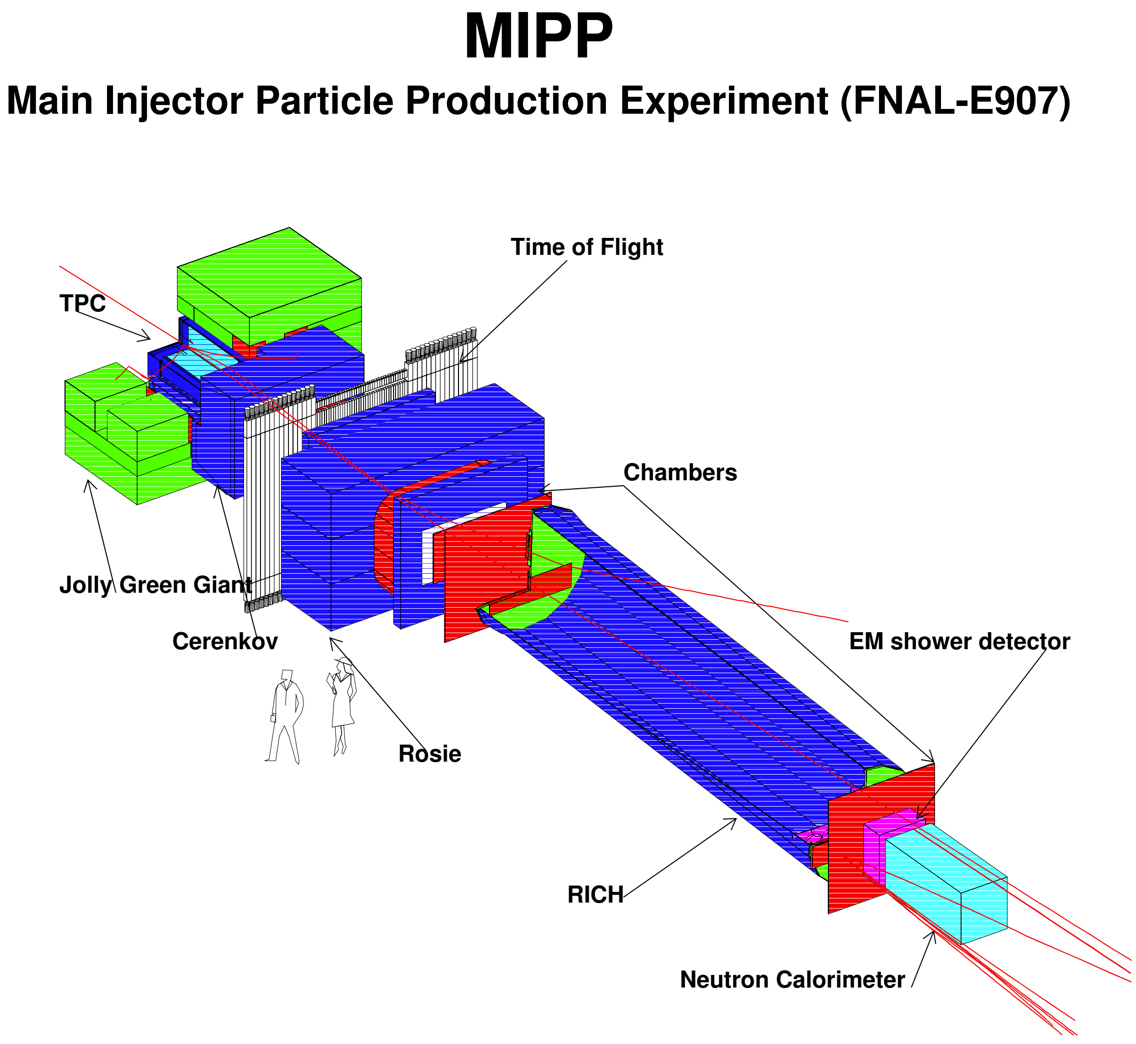

Figure 2.1: The cut view of the MIPP spectrometer.

The particle tracking was achieved with three beam chambers, a time projection chamber, four drift chambers, and two multi-wire proportional chambers. Three beam chambers provided beam particle trajectories through the Beam Čerenkov counters and the target with a precision less than 0.4 mm. The Time Projection Chamber provided low momentum secondary particle tracking.

The downstream tracking was done by four drift chambers and two multi-wire proportional chambers. Each detector has four sensitive planes and provided secondary particle tracking with resolution less than 1 mm. The wires in the different planes were oriented in different ways: u, v, u', and v' views (±7.93 and ±21.6 degrees wrt. vertical) for the drift chambers and horizontal (measuring y), vertically (measuring x), and at angles of ±28.07 degrees with respect to the y direction for the proportional wire chambers.

The magnetic fields of two analyzing magnets were set to 0.7 Tesla and -0.6 Tesla in y direction and the magnets deflected charged particles in opposite directions. The fields were mapped on $2''$ grids with uniformly separated points.

The particle identification was done using two beam Čerenkov counters to tag the beam particles as pions, kaons, and protons of both charges, the Time Projection Chamber to determine low momentum charged secondary particles of electrons, muons, pions, kaons, protons, and deuterons less than 1 GeV/c, the threshold Čerenkov counter to identify charged secondary particles between 3 GeV/c and 20 GeV/c, the Time of Flight wall between 1 GeV/c and 3 GeV/c, the Ring Imaging Čerenkov counter to separate up to 90 GeV/c, the electromagnetic and hadron calorimeters to detect respectively forward going photons and neutrons.

2.2 Beamline

MIPP uses two types of beam: 120 GeV/c primary proton beams and secondary beams of π, K, p in the momentum range of between 5 and 90 GeV/c.

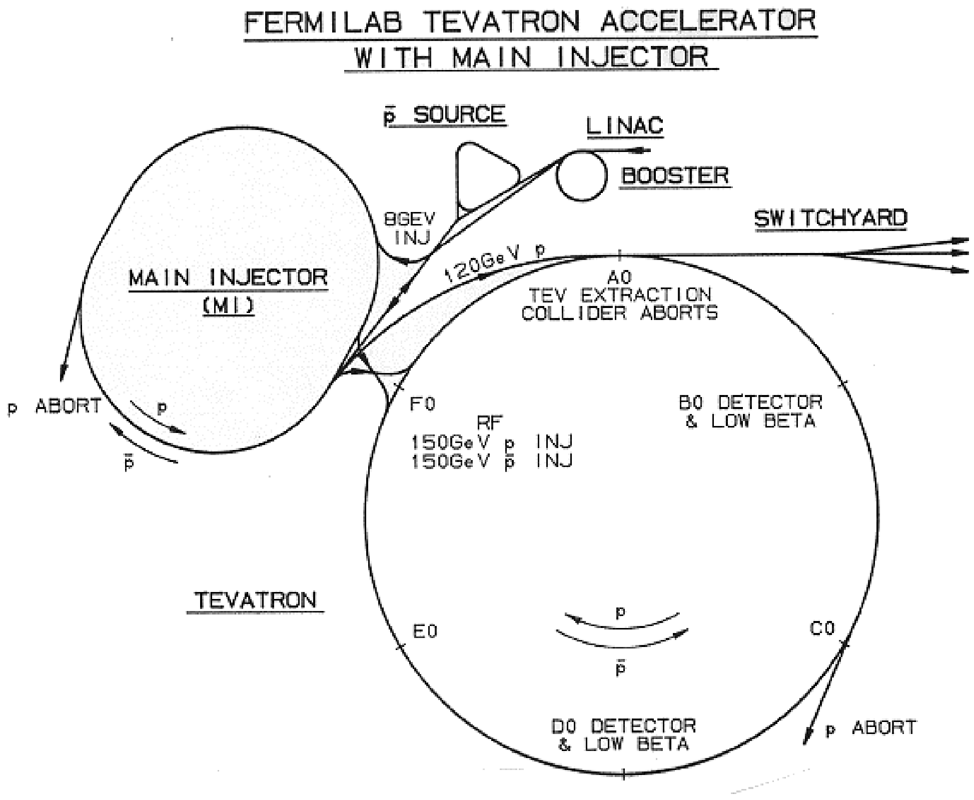

Figure 2.2: FNAL Accelerator.

Primary proton beam is extracted from the Main Injector. As shown in figure 2.2, protons are accelerated up to 8 GeV/c at the LINAC and the Booster. Then, Main Injector RF cavities accelerates protons up to 119.7 GeV/c. Later, accelerated protons are sent through Switchyard to be split between the Meson Test (MT) area and the Meson Center (MC) area. The MIPP experiment is located in the MC7 hall. For the analysis presented here the primary target in the beamline was removed and the primary MI proton beam was transported directly onto the experimental target. Beam was delivered in slow-spills of 4 second duration at intervals of 2 minutes.

Secondary beams are obtained by allowing primary beam to interact with a 0.5 cm x 0.5 cm copper target mounted at the entrance of the MC6 area, which is at immediately upstream of the MC7 area. Two dipole magnets in the MC5 area at the upstream of the target bends proton beam towards the target. Two other

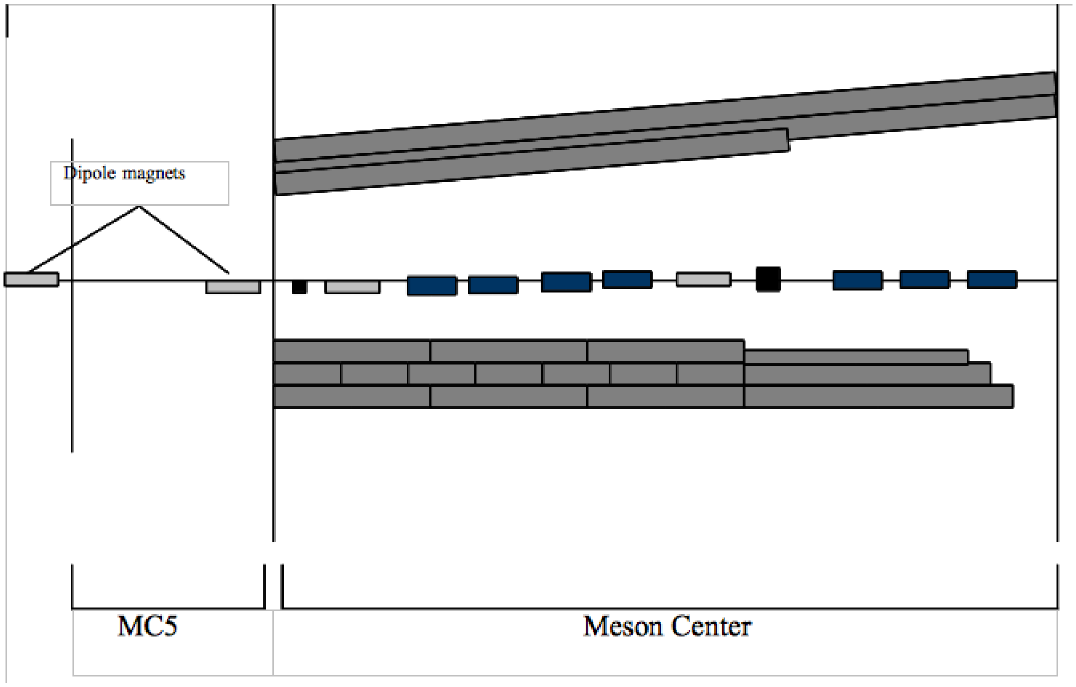

Figure 2.3: Secondary beamline layout.

dipole magnets at the downstream of the target focuses the secondary beam produced at the target onto the beamline center. Four quadruple magnets between the downstream dipoles were used to bring the secondary beam onto a jaw collimator. The vertical aperture of the collimator can be varied so that δp of the beam can be set. The central momentum value of the beam was set up by the strengths of the two downstream dipole magnets. Finally, the beam after the collimator was refocused to the beamline center and to the experimental target by an additional three quadruple magnets. The layout of the secondary beamline is shown in figure 2.3.

2.3 Targets

Targets used in the MIPP were of three parts: nuclear, cryogenic (liquid hydrogen), and NuMI. Also, an empty nuclear target and an empty cryogenic target were used to determine backgrounds. This analysis used data from the thin carbon target only. The p-p interactions on LH_2 were used in calibrating the detector. The NuMI target is described because the measurements on thin carbon were in part motivated by the NuMI target design.

2.3.1 Nuclear Targets

MIPP nuclear targets were 5 cm in diameter and mounted on a target wheel. The target wheel was installed a few centimeters upstream of the front face of the TPC and could be rotated by a computer controlled motor. This option allowed targets to be changed without accessing the MIPP experimental hall. Atomic weights of the nuclear targets were between 9 and 238, so MIPP could investigate nuclear interactions over a wide range of atomic weights. The other main properties of the nuclear targets are shown in Table 2.1.

Table 2.1: Target properties.

target	mass $[g]$	thickness $[cm]$	areal density $[g/cm^2]$	inter length [%]	rad legth [%]
Aluminum	21.4	0.399	1.056	0.992	4.4
Beryllium	14.4	0.399	0.715	0.95	1.1
Carbon	16.6	0.498	0.819	0.94	1.9
Carbon2%	34.0	1.003	1.667	1.94	3.9
Bismuth	34.25	0.173	1.690	0.87	27
Silver	62.6	0.294	3.088	3.15	10
Copper	26.6	0.152	1.31	0.97	10
Uranium	38	0.1	1.875		

2.3.2 Cryogenic Target

The Cryogenic target used at MIPP is filled with liquid hydrogen and controlled through the iFix/APACS system, which generally controls the pressure and temperature of the gas systems. The target cell is approximately a cylinder of 1.5 inch (3.8 cm) diameter and 14 cm length. There are caps bulged out on each end of the target, so that they could hold the pressure. The caps are not flat and the exact target length is a function of the radius. The total cryo-target system holds 0.2 liters of liquid hydrogen. The volume the target cell is approximately 0.16 liters. The temperature and the pressure of the target were monitored continuously. Although there were some operational fluctuations, the average volume density of the target can be estimated as 0.070 g/cm^3, so the areal density is around 1 g/cm^2.

2.3.3 NuMI Target

The NuMI target used at the MIPP is the same as used at the MINOS experiment. The target is made of graphite with a density of 1.78 g/cm^3. The main target consists of 47 target segments, which are placed vertically. Each segment is 20 mm in length, 6.4 mm in width, and the distance between target segments is 0.3 mm. The target canister is filled with helium gas for providing heat transfer from the aluminum casing, which covers the target segments, to cooling water pipes. A 48th target segment is installed at the upstream end of the target segments horizontally for providing a cross check of the position of the target. The NuMI target and the target vacuum canister are shown in Figure 2.4. The detailed information about the NuMI target can be found in reference [6].

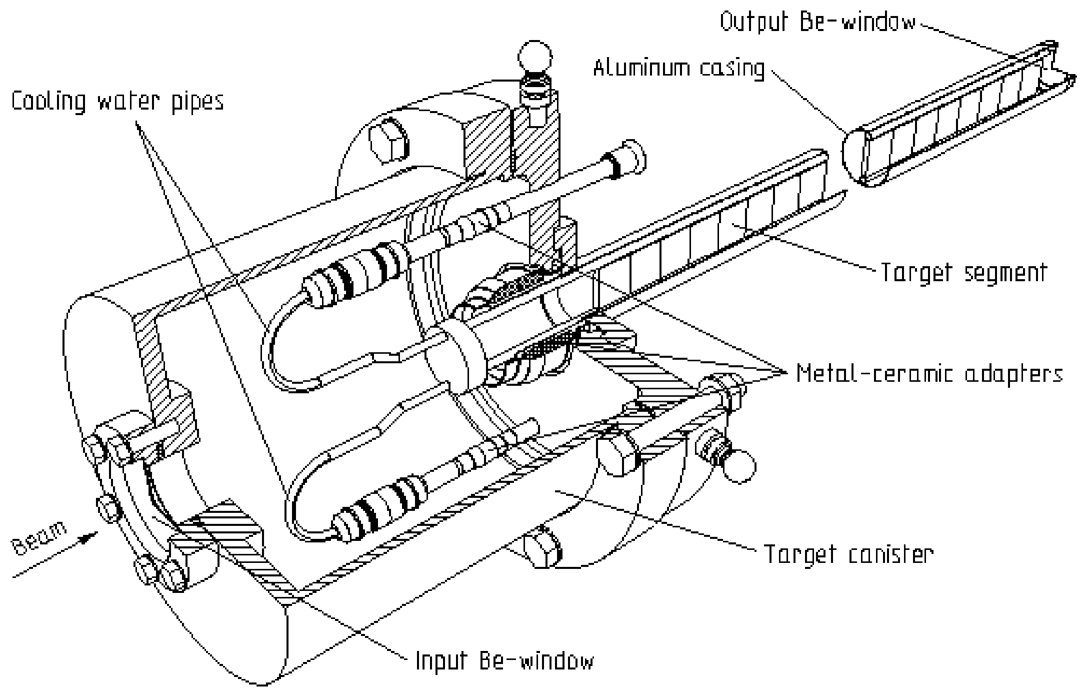

Figure 2.4: NuMI Target.

2.4 Detectors

2.4.1 Drift Chambers

MIPP used three small drift chambers (BC1, BC2, BC3)[10] to measure incident beam particle trajectories and four larger drift chambers (DC1, DC2, DC3, DC4) located downstream of the target for tracking of the particles from the interactions in the target.

All drift chambers have four planes of wires with the wire angle orientations of ±21.60 degrees on plane 1 and 4 and ±7.93 degrees on plane 2 and 3 with respect to the vertical (y-axis) direction.

The Beam Chambers are identical and have 160 wires per plane with 1 mm wire spacing. The chambers have an active area of 15.24 cm x 10.16 cm and were filled with the gas mixture of Ar/C_4H_{10}/methylal in proportions of 82:15:3.

DC1 has 512 wires per plane with 3.5 mm wire spacing. DC2, DC3, and DC4 have 512 wires on planes 1 and 4 but 448 wires on planes 2 and 3 with 3.175 mm wire spacing. The active area of the DC1 is 182.88 cm x 121.92 cm while the others (DC2, DC3, DC4) active areas are 152.4 cm x 101.60 cm. The wire planes in the chambers were separated by a distance of 0.7 cm. The larger drift chambers were filled with the gas mixture of argon, C_4H_{10}, and methylal in ratios of 69:28:3.

The signals from the planes of the chambers are amplified by 8-channel preamplifiers, discriminated by 32-channel Nevis discriminators, and the drift time is measured by a 4290 CAMAC TDC system with 1 ns resolution.

2.4.2 Multiwire Proportional Chambers

Two identical multi-wire proportional chambers (PWC5 and PWC6) were placed immediately behind and in front of the RICH detector to provide 3D trajectories of high momentum charged secondary particles.

The chambers have an active area of 2 m x 2 m and a length of 40 cm along the beam direction. The details of the chamber construction can be found in reference [12]. The chambers each have four planes of wires. Each plane has 160 tungsten anode sense wires with 3 mm wire spacing. The anode wire planes are oriented in four different ways: vertical, horizontal, and with angles of ±28.070 degrees with respect to the vertical direction. The schematic for anode wire orientations is shown in Figure 2.5. The gas mixture used in the chambers is $Ar/CH_4/CF_4$ in proportions of 76.5:8.5:15. During the data taking two planes in PWC5 could not hold high voltage, but due to the high redundancy in the tracking system this did not affect the data reconstruction significantly.

The chambers were read out by the RMH electronics [17]. The signals from the anode wires were amplified by the 32-channel pre-amps and discriminated by a total of 160 32-channel RMH modules located in 8 CAMAC crates.

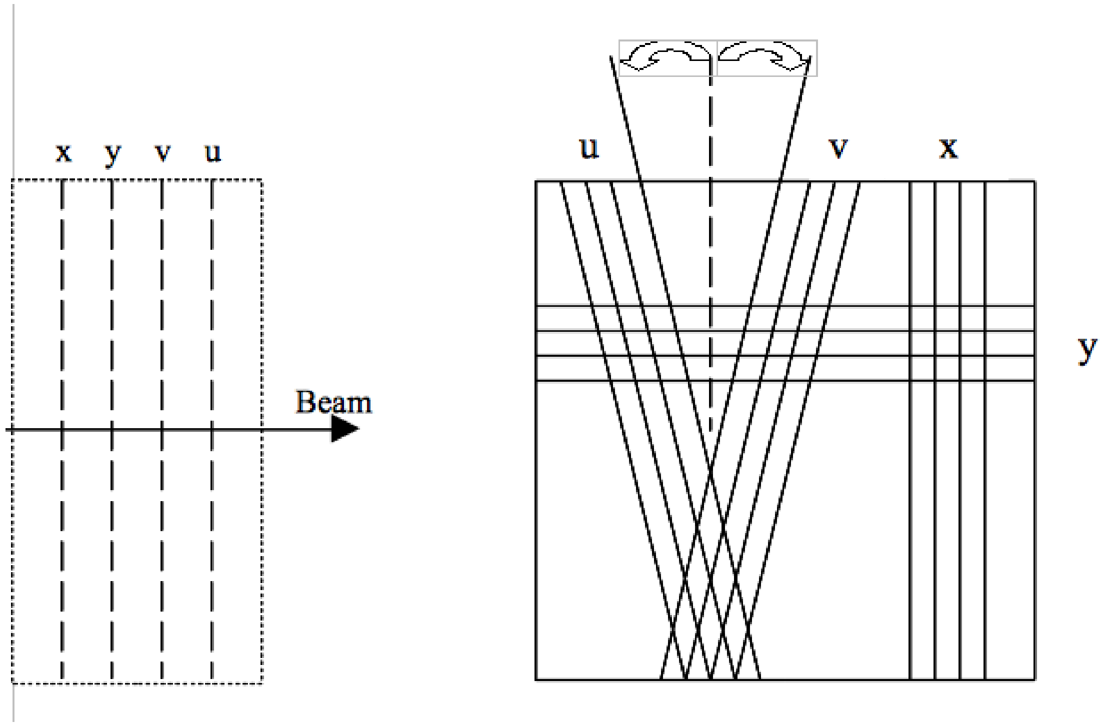

Figure 2.5: MWPC Anode wire orientations.

2.4.3 Beam Čerenkov

Two beam Čerenkov counters located upstream of the experimental target provided tagging of the incident beam particles. Each counter has a cylindrical radiator volume and a head with two PMTs at the downstream end. The radiator volume lengths are 22.9 m and 12.2 m for the upstream and the downstream counters, respectively. In the head, a focusing mirror reflects the Čerenkov light onto a second mirror, which contains a hole. The light emitted at angles below the cutoff value hits the "inner" PMT behind the second mirror. If the light is emitted at larger angles than the cutoff, it is reflected by the second mirror towards the "outer" PMT. The cutoff angle is 5 mrad for the upstream counter and 7 mrad for the downstream counter.

Beam particles are identified using the counters by taking account of the fact that, at the same momentum, particles with different masses create Čhrenkov light at different angles. To tag beam particles, the density in the upstream counter was chosen for each beam momentum in such a way that the pion Čerenkov light hits only the outer PMT. The kaon light at the same momentum hits the inner PMT only, and protons do not radiate. The gas density in the downstream counter was set so that, only protons radiated. The proton Čerenkov light hits the inner PMT and misses the outer PMT. At 120 GeV/c the beam consists of protons only and beam pid was not needed. The 1^{st} counter BCkov was evacuated to reduce multiple scattering in the beam and the 2^{nd} BCkov was set to identify protons to reduce background in the beam. Above 30 GeV/c beam momentum, the counters were filled with nitrogen. However, the density of the nitrogen was not enough to allow identification of protons below 30 GeV/c or kaons below 20 GeV/c. Therefore, a heavy non-flammable gas of C_4F_8O was used below 30 GeV/c beam momentum.

2.4.4 Time Projection Chamber

The Time Projection Chamber (TPC) was used to provide 3D particle tracking and particle identification of secondary particles with energy loss at low momentum. It was previously used for the EOS experiment [14][11][20][9] at the Lawrence Berkeley Laboratory and in the Brookhaven Lab E910 experiment.

The TPC was located inside the Joly Green Giant (JGG) magnet and the MIPP target was placed just upstream of the active volume of the TPC inside the TPC ‘optics bay’ used for optical calibration systems in previous experiments. The gas volume of it is 96 x 162 x 81 cm^3 filled with the P10 gas (90% Argon with 10% CH_4). The working principle of the TPC is based on the ionization of the P10 gas while the particles from the target are traveling through the gas. Ionization electrons travel to the bottom of the chamber, and the positive ions drift to the cathode plane on the top of the chamber under a uniform electric field of 125 V/cm. The electrons pass through three wire planes while they are drifting to the bottom:

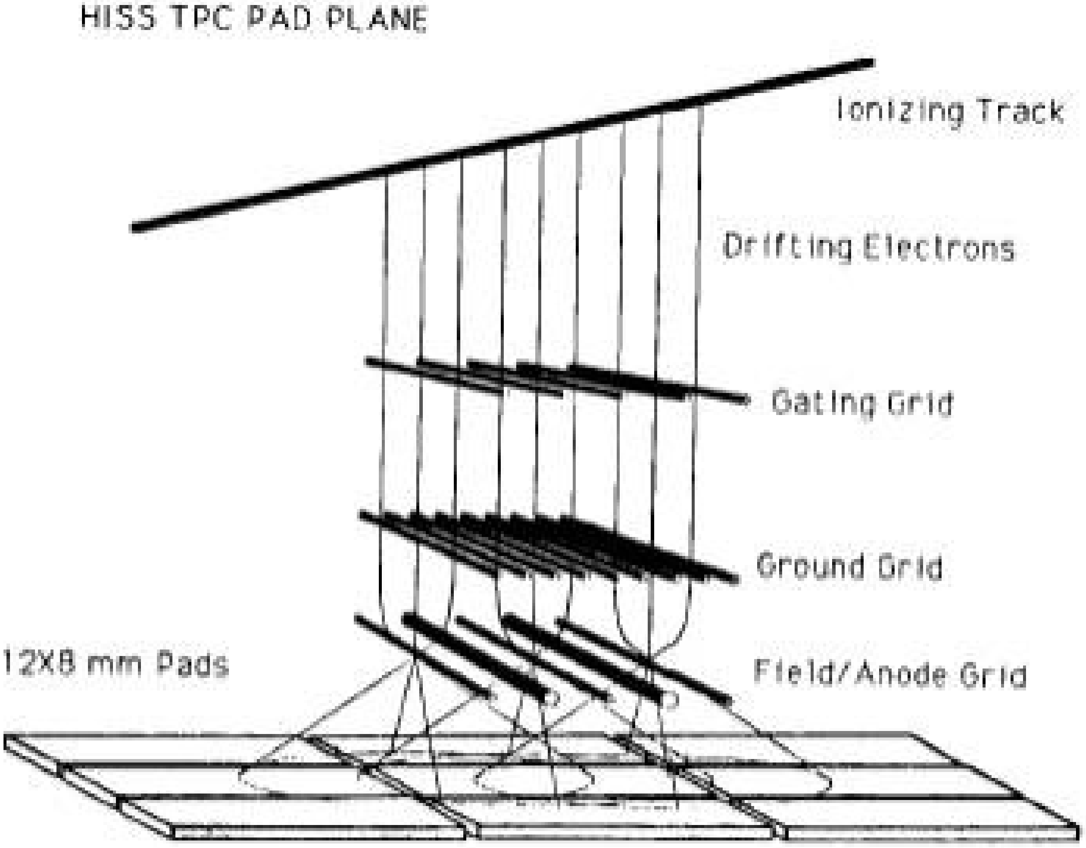

Figure 2.6: Schematic view of the TPC pad plane with anode and ground wires.

gating grid, ground wire plane, and anode wire plane. The region between the ground wire plane and the anode wire plane is the amplification region, and when the electrons reach this region, an avalanche occurs. This avalanche creates an image charge on the readout pad plane 4 mm below the anode wire plane. The wire and pad plane schematic is shown in figure 2.6. The pad plane consists of 128 pad rows along the beam direction and 120 pad columns in the x direction. Each pad is 12 mm in length and 8 mm in width. The active pad plane area is 96 cm in width along the x axis and 153.6 cm in length along the beam direction (z axis). The x and z position of track hits are given by the pad plane and the y position is provided by drift time. Since the drift velocity of electrons is approximately $5cm/\mu s$ and the readout rate is 10 MHz, the y direction is divided into 160 5 mm and 100 ns time

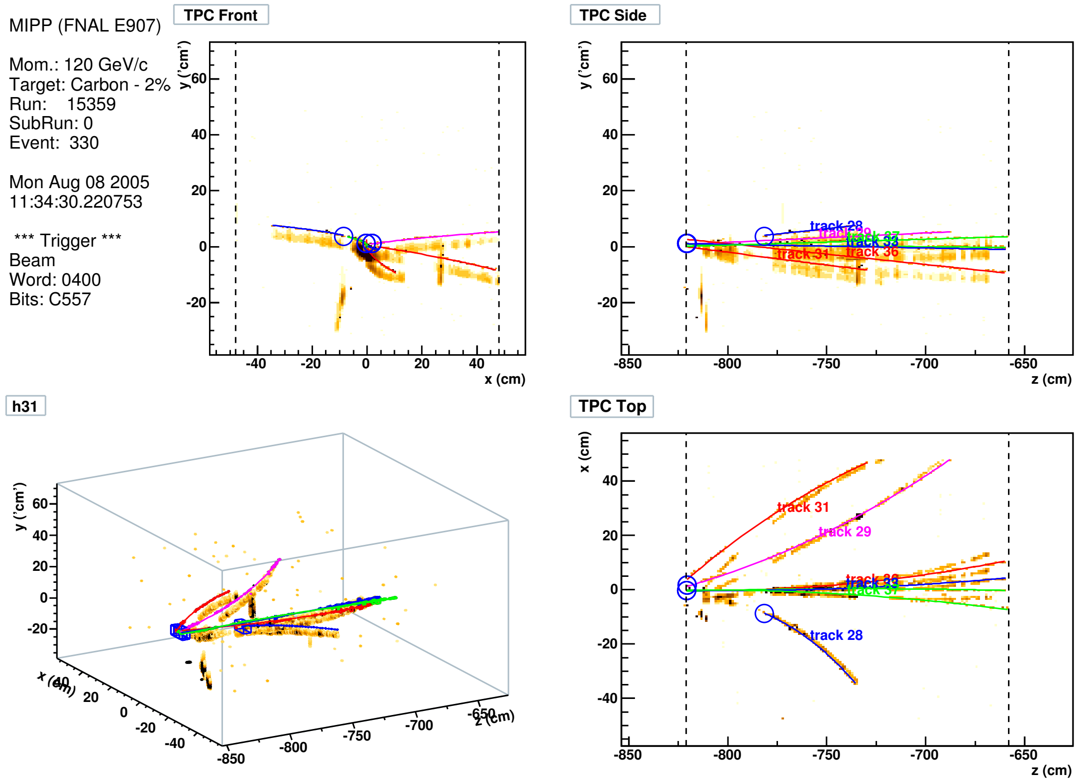

Figure 2.7: Event display from the TPC. Grey colored are the raw hits, solid lines are the reconstructed particle trajectories.

buckets.

The TPC electronics consists of sticks underneath the pad plane for preamplifying and shaping of the signals, ADC modules for digitizing, and dedicated VME boards connected to sticks by fiber optics for interface to data acquisition processors. An event display from the TPC detector is shown in figure 2.7.

2.4.5 Time of Flight Wall

The Time of Flight (ToF) wall used in MIPP is located immediately upstream of the ROSIE analyzing magnet to identify secondary charged particles with momentum between 1 and 3 GeV/c. The wall consists of 54 3 m long scintillator bars. 40 smaller 5 cm x 5 cm bars are at the center while 10 cm x 10 cm bars are at the sides of the detector. The total width of the wall is 3.5 m. Each bar is readout by two PMTs (Hamamatsu R5099U) placed on the top and the bottom of the bar. The ToF measures the arrival time of the particles reaching into the scintillator bars with multiple hit CAMAC TDCs. The system achieved approximately 180 ps resolution for beam particles. The time of flight is measured relative to a T0 given by the T0 counters, a set of three scintillators in the beam line used to determine the time of an interaction as well as to detect beam particles for the trigger system.

2.4.6 Threshold Čerenkov

The threshold Čerenkov counter is located immediately downstream of the first drift chamber and is followed by the second and the third drift chambers. It was used to separate charged secondary particles originated from the target in the momentum range between 3 and 20 GeV/c. The radiator gas used in the counter was C_4F_10 with the density of 10.12 g/l (i.e. atmospheric pressure at room temperature). The gas has momentum thresholds of 2.6 GeV/c for pions, 8 GeV/c for kaons, and 17 GeV/c for protons. The counter box is 2.8 m wide, 3.3 m high and 1.1 m long. The active volume of the counter consists of 96 toroidal mirrors at the downstream end mounted on two plates as shown in figure 2.8. The mirrors are in three different sizes: 6” x 6.928”, 12” x 13.856”, 12” x 9.660”. The smaller mirrors are placed at the central part of the counter. 96 PMTs at the top and the bottom wall of the counter are individually matched to the mirrors. The alignment of the mirrors was done in such a way that Čerenkov light is reflected onto only one PMT if particles originate at a certain focal length in front of the Čerenkov counter. More information about the counter is documented in reference [15]. The charge of the PMTs was digitized with LeCroy 4300 ADC modules, and LeCroy 3377 multi-hit TDCs recorded hit times of the signals.

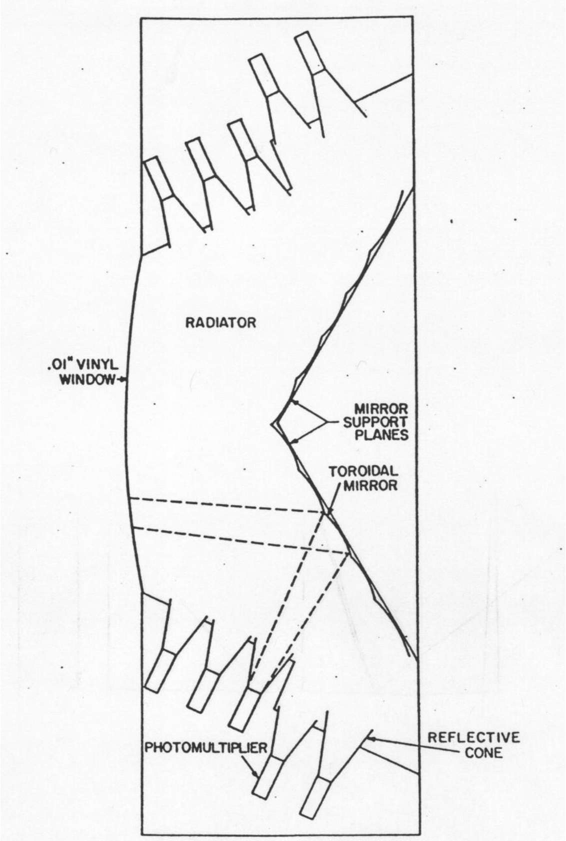

Figure 2.8: Schematic view of the Čerenkov counter.

2.4.7 Ring Imaging Čerenkov Counter

The Ring Imaging Čerenkov (RICH) counter was previously used in the SELEX experiment. The RICH is a cylindrical vessel with a radius of 1.17 m and a length of 10 m. In MIPP, the radiator volume was filled with CO_2 gas at room temperature and a pressure kept between atmospheric pressure and 15.1 psi. The vessel contains 16 hexagonal spherical mirrors placed at the downstream end to reflect the Čerenkov light onto 2848 hexagonally close packed 0.5 inch diameter PMTs at the upstream end above the beam window. The average focal length and the radius of the mirrors are 9.9 m and 19.8 m, respectively. Since the image of the Čerenkov light at the PMTs has a ring shape, and particles with the same momentum but different masses create rings at different radii, measuring the ring radius by the PMT provides particle identification of the charged particles traveling through the RICH.

Two types of PMTs were used in the RICH. One is the Hamamatsu R-760 with a quartz window and the other one is the FEU-60 with a glass window covered by a wavelength shifter. The efficiency of the FEU-60 PMT is only about 36% but it is cheaper than the Hamamatsu tubes.

The readout electronics consists of front-end cards and custom VME boards. The signals from the PMTs are read out by 89 32-channel front-end cards. Each channel in a card contains a differential amplifier and an analog comparator. The discriminated signals are then sent to VME boards.

The figure 2.9 is an online event display showing hit PMT's in the PMT base.

2.4.8 Electromagnetic Calorimeter

The electromagnetic calorimeter is mounted at the downstream end of the MIPP spectrometer immediately before the Hadron calorimeter to detect forward going high momentum photons and to measure their energies. The active volume of

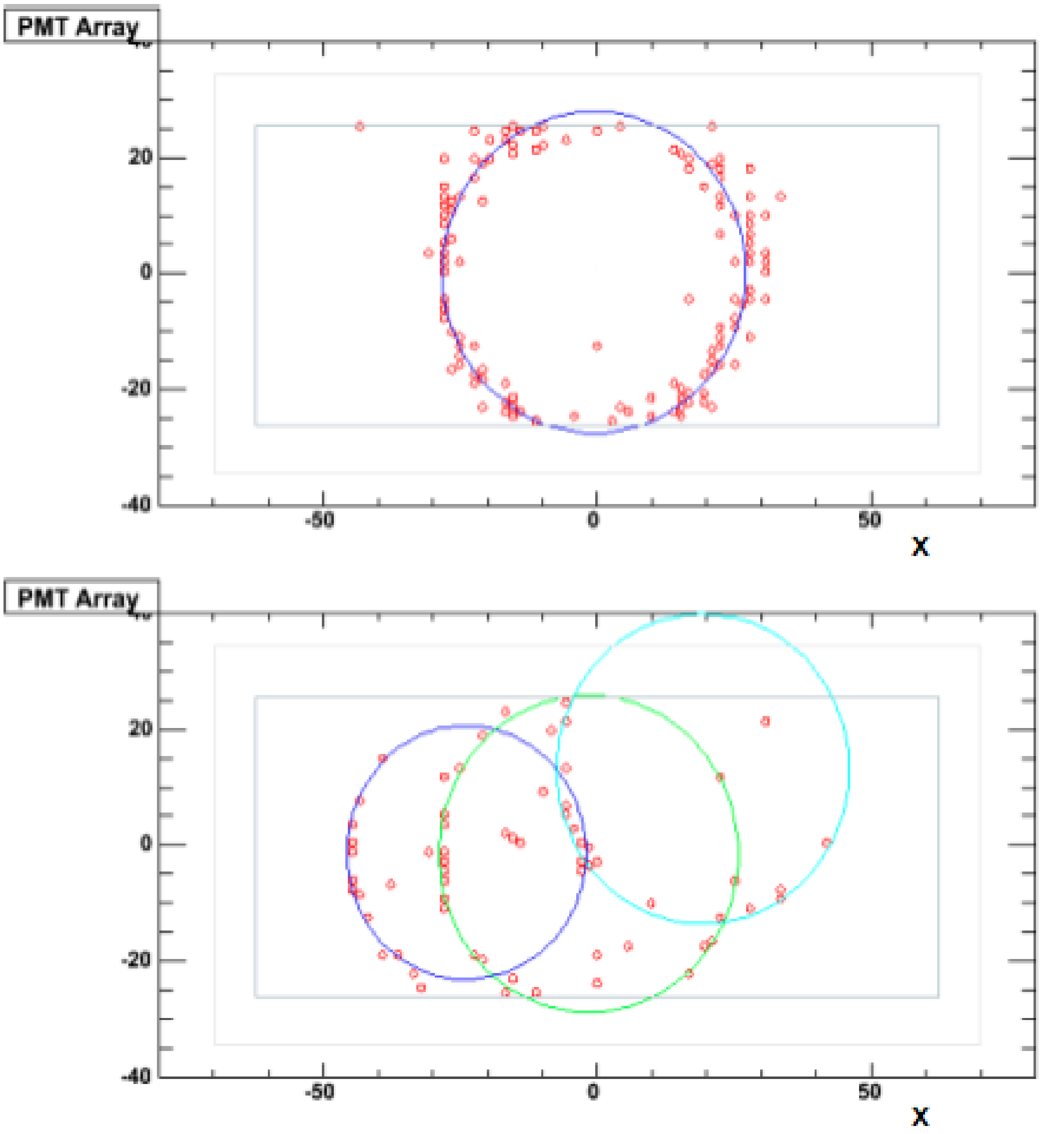

Figure 2.9: RICH online event display. Small red circles indicate PMT hits. Large circles are fit by reconstruction software. Top: single beam particle event; Bottom: interaction event.

the calorimeter consists of 10 planes of proportional wire chambers attached to 5.08 mm thick lead sheets. Each active plane has eight 8-inch wide, 1-inch thick wire chambers oriented horizontally and vertically alternately. Each chamber contains 8 anode wires with 25.4 mm wire spacing. The chambers are filled with the gas mixture of P10 (90% argon and 10% methane) and CF_4 in proportions of 86: 14. The EMCAL is read out with custom ADC CAMAC units built by the University of Michigan group.

2.4.9 Hadron Calorimeter

The Hadron Calorimeter (HCAL)[13] is the last detector in the MIPP spectrometer situated directly behind the EMCAL and used to identify and measure the energies of the forward going neutrons. The HCAL consists of 64 layers of iron sheets with 24.1 mm thickness and four 5 mm thick scintillator plates placed between steel plates. The active volume of the calorimeter is 0.99 m in width, 0.98 m in height, and 2.4 m in length along the beam direction. The length of the calorimeter corresponds to 88.5% radiation length and 9.6% interaction length. The side view of the EMCAL and HCAL together is shown in figure 2.10.

For readout purpose, each scintillator plate is divided into two cells symmetric about the vertical plane through the beam axis and each cell is read out by one PMT. The signals from the PMTs are read out by custom ADC CAMAC units built at the University of Virginia. The calibrations and some studies showed that the EMCAL and HCAL have a linear response with respect to the beam particle energy. The energy resolution is approximately 10%, which is expected from a sampling calorimeter.

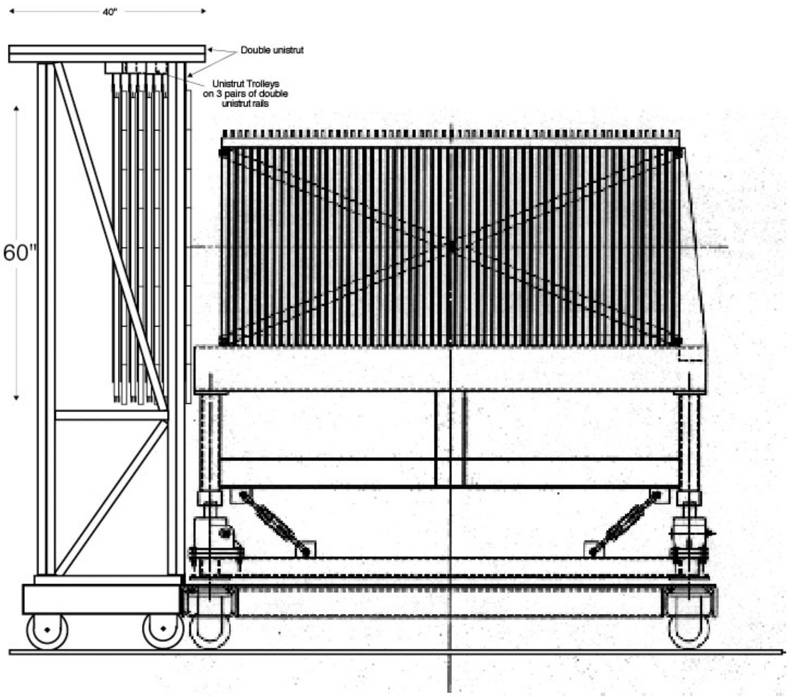

Figure 2.10: The side view of the EMCAL(left) and HCAL(right).

2.5 Magnets

The MIPP has two analyzing magnets with the fields in opposite direction: Jolly Green Giant (JGG) and Rosie. The JGG surrounds the target and the TPC to be used for measuring momentum of the low momentum charged particles. The Rosie is placed between the ToF counter and the last drift chamber and is used for high momentum measurements. The Ziptrack devices were used to map out the magnetic fields of both the JGG and the Rosie. The x, y, and z components of the magnetic fields were measured in a 2” cube grid of points. The magnetic fields are not uniform. The x and y components of the JGG field are about 20% of the z component on average. This caused upto 7 cm distortion on particle trajectories in the TPC. Therefore, distortion correction was applied on the TPC hit points using the field map during the reconstruction stage to obtain true hit positions. The magnetic field of the Rosie is more uniform than that of JGG.

CHAPTER 3
THE MIPP TRIGGER SYSTEM

The MIPP trigger system is a single-level trigger system, which consists of a set of scintillation counters and trigger detectors. The main goals of the MIPP trigger system are to select beam particles with high probability, to tag beam particle and to decide whether or not beam particles had an interaction with the target. These goals are achieved using 7 physics trigger bits: beam identification, three beam particle identifications (pion, kaon, and proton), and three beam particle identifications with interaction. Each trigger bit is prescaled differently to select 20% minimum bias triggers and 80% interaction triggers. Another criterion when setting the trigger prescales is to have the same amount of each beam species, since beam spills have much fewer kaons than protons and pions. For 120 Gev/c beam only the beam identification, proton beam pid, and proton interaction trigger bits were used.

Since the TPC is the most complicated detector for the readout system, it limited the trigger rates. The trigger rate was 20 Hz in events with many tracks and up to 60 Hz in simple events. The information for the MIPP trigger system can be found at [4].

3.1 Beam Identification

In the MIPP Trigger System, beam particles (BEAM) are defined by the coincidence of the TBD and T01 scintillation counters in the MIPP beamline and the anticoincidence of the Veto counter.

$$BEAM = TBD \cdot T01 \cdot \overline{Bveto} \tag{3.1}$$

The triggers from the TBD and T01 are formed by the coincidence of three of the four discriminated PMT signals.

The BVeto counter is a piece of scintillator with a 4.32 cm diameter hole, which is mounted 140 cm upstream of the target, close to the T01 counter. Since the TBD and the T01 counters have larger areas than the target, the BVeto counter selects beam particles on the target. It also vetoes events from beam halo.

3.2 Beam Particle Identification

Beam particle identification was achieved by the two beam Čerenkov counters. Above 20 GeV/c beam momentum, the pressure in the beam Čerenkov counters was selected such that all charged particles radiate light. The two PMTs in each counter were named as 'inner' and 'outer'. The pressure in the counters was set according to beam momenta such that the standard beam particle identification is given by

$$\begin{aligned} \pi &= \overline{BCkov1_{in}} \cdot BCkov1_{out} && (3.2) \\ K &= BCkov1_{in} \cdot \overline{BCkov1_{out}} && (3.3) \\ p &= BCkov2_{in} \cdot \overline{BCkov2_{out}} && (3.4) \end{aligned}$$

where BCkov1 is the upstream and BCkov2 is the downstream counter.

At 5 GeV/c beam momenta, it is not possible to identify protons and kaons using the beam Čerenkov counters because protons with momentum below 20 GeV/c and kaons with momentum below 11 GeV/c could not emit light in the counters. At 5 GeV/c beam momenta, protons and kaons can be identified offline by measuring the time of flight of the particles between T00 and T01. Only proton beam pid was used for 120 GeV/c beam

3.3 End of Spill and Calibration Triggers

The end of spill trigger in MIPP is used to read out scalers for each beam spill. During the read out, the detectors were not triggered and the numbers from the scalers were written to the database.

The scalers counted the number of raw trigger bits, gated raw trigger bits, prescaled trigger bits, prescaled and gated trigger bits. Basically, there are 20 trigger bits: One for untagged beam, three for tagged beam, three for tagged beam with interaction, one for DC1 interaction, one for Scinteraction Hi, one for T01, one for TBD, one for the inter-spill calibration pulser, and others, that are reserved for different run configurations.

Calibration triggers are formed using a pulse generator to trigger detectors. The calibration triggered events are used to calculate pedestals and noisy channels in detectors. Calibration triggers were issued between beam spills.

3.4 Interaction Trigger

MIPP used the first drift chamber (DC1) as a multiplicity interaction trigger requiring at least two hits in at least three of the four planes. Later, the scintillation interaction counter was installed and used with DC1 to form the interaction trigger. The problem with the DC1 was that a lower discriminator threshold and noise reduced the purity of the trigger.

3.4.1 Scintillation Interaction Counter

The scintillation interaction trigger counter is a 5.40 x 7.62 cm piece of plastic scintillator with 3.175 mm thickness mounted 1.5 cm downstream of the experimental target. It is sandwiched between two aluminum brackets at the top and bottom and two aluminized Mylar sides. The interaction length and the density of the counter are 81.9 g/cm^2 and 1.032 g/cm^3, respectively. Its thickness of 3.175 mm corresponds to 0.4 interaction length. 191 1.2 mm diameter fibers are connected at each side of the counter and the other edges of the fibers are gathered into two bundles along the beam axis. These bundles are connected and glued to a

Burle 83054H PMT, which produces approximately 73 photoelectrons per minimum ionizing particle (mip).

The scintillation counter forms two trigger bits: SciHi and SciLo. SciHi and SciLo are created for the ADC threshold settings ∼3 mip and ∼1.5 mip, respectively. For the physics runs SciHi was used as an interaction trigger since single particle energy deposition distribution has long Landau tail, and for SciLo threshold, most of the uninteracted beam particle events would form an interaction trigger.

CHAPTER 4
EVENT RECONSTRUCTION

4.1 Offline Framework

The MIPP offline software is based on C++ and ROOT. The MIPP also uses several external packages such as PostgreSQL to handle input data from various sources, CVS(Software Version Control) to share code and to manage versions, SRT(Software Release Tools), which is a Fermilab program for code release management. Another package of Xerces C++ is used to handle XML files.

In MIPP, DAQ(Data Acqusition System) stores raw data from each detector. For offline analysis, the raw data is converted to ROOT format. Then, software packages run over ROOT files.

4.2 Track Reconstruction

The track reconstruction in the MIPP can be divided into two parts: Finding particle trajectories using wire chamber measurements and reconstruction of tracks in the TPC.

To find tracks using wire chambers, the chambers first are grouped into triplets: BC123, DC123, and DC4/PWC56. The triplets are separated by the JGG and Rosie analyzing magnets. In each chamber, straight line track segments are searched for. To do that, in the planes of the chambers, wire clusters are formed using the wire digit information. For the drift chambers, the times of the digits in a given cluster must be compatible and the size of a cluster is limited to two. After finding clusters, the next step is to build wire crosses.

Wire crosses are the combination of the wire clusters from different planes in a chamber. Initially, two cluster combinations from different planes are obtained and intersection of the clusters are calculated. Then, the clusters in the other planes are added to the cross if their positions are consistent with the intersection of the initial two cluster combination.

The straight line track segments search is similar to the wire cross finding. For that, in each triplet, all possible two wire cross combinations from different chambers are found. The crosses which are not compatible in time are thrown out. Acceptable combinations are fit to a 3D straight line and the position in the other chamber is predicted. The crosses that are compatible in time with the first two crosses and whose positions are consistent with the predicted position are added to the straight line segment.

Once all track segments are found, 6-chamber track candidates are constructed with the segments in the DC123 and DC4/PWC56 triplets. The positions of the segments in both chamber groups are extended to the center of the Rosie magnet, and they are matched if their x and y positions are consistent. Matching segments are defined as 6-chamber track candidates. The track candidate is fitted with the template track fitting method. The χ^2 of the fit determines if the track is to be accepted or not. The template track fitting has five parameters for a given track: q/p (charge and momentum), x and y position, and the angles of dx/dz and dy/dz. The fig 4.1 shows the event display for the global track reconstruction. Blue circle and stars indicate wire chamber clusters and crosses.

4.2.1 TPC Track Reconstruction

The TPC track reconstruction starts with forming 2D clusters on each pad row. A pad row, pad column, and a time bucket in the TPC volume define a voxel. So neighboring voxels with digits in the xy plane define a cluster.

Mostly, a cluster involves multiple hits. This is because the TPC read out is sensitive to out-of-time tracks or tracks that are close to each other. To find all hits in a cluster, multiple peaks are formed. Peaks are defined as a set of ADC digits on

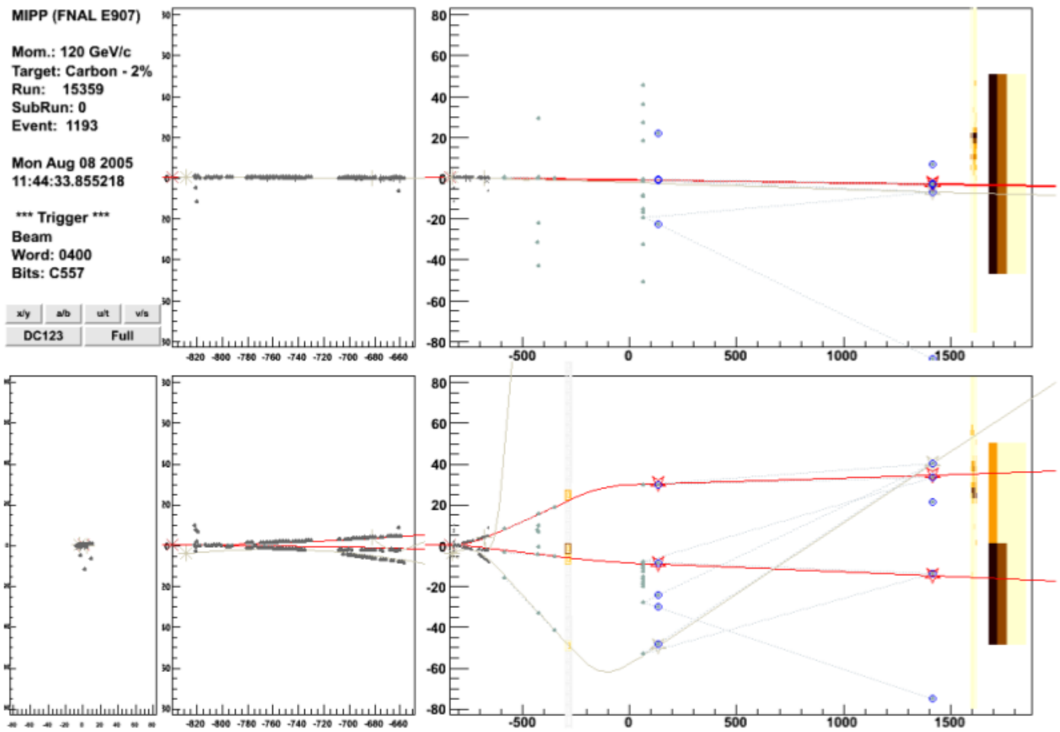

Figure 4.1: Event display for a reconstructed global track.

a single pad, whose time distribution can be fit to the gamma function.

Once peaks are found, the charge distribution of them as a function of time is tried to be fit to the Gamma function, which is defined as

$$q(t) = A\left(\frac{t}{\tau}\right)^{\gamma-1} exp\left(-\frac{t}{\tau}\right) \tag{4.1}$$

where τ and γ are parameters taken from TPC electronics.

The function to be minimized over total number of N digits in a peak is

$$\chi^2 = \sum_{i=0}^{N}[lnq_i - lnq(t_i)]^2\omega_i \tag{4.2}$$

where ω_i is the weight for an ADC digit, which is the square of the ADC value.

If the peak is successfully fit, then the peak time is the most probable value (MPV) of the fit function. Otherwise, the peak time is the ADC value weighted mean of the time distribution of the digits in the peak.

Once peaks are found, then hits are formed. A hit is defined as a group of peaks on neighboring pads whose peak times are within 2 time-buckets of each other. A hit requires at least two peaks.

Tracks are formed by connecting the closest hits in the neighboring pad rows. Track reconstruction starts at the downstream end of the TPC. The closest hits are fit and the position is predicted in the other pad rows. The hits that are consistent with the prediction are added to the track. The details of the TPC track reconstruction algorithm can be found at [16].

4.3 Vertex Reconstruction

The MIPP Vertex Reconstruction package was achieved using the deterministic annealing method (DAM), which is based on a root minimization class. To manage this, all reconstructed beam and secondary tracks are stored in an array. If there is no outgoing track in an event, vertex finding is not activated; otherwise the vertex package is started to find vertices.

The algorithm finds a point at which the sum of weighted square distance of tracks is minimum. ROOT Minuit package performs seven iterations. For each iteration, tracks are weighted according to the formula

$$trackweight = \frac{1}{1 + exp\left((rsqr - rcsqr)/(2T)\right)}, \tag{4.3}$$

where rsqr is the square of the radial distance between tracks and the point which is taken as the vertex position, rcsqr is the square of the critical distance between tracks and the vertex position that was set to 9 cm^2. It indicates that at T=0, only tracks within that distance are used for the vertex position calculation, and T is the temperature which take values between 5000 and 0.1 cm^2 . The weight of the beam tracks was also scaled by a factor of two since their position resolution is better than that of secondary tracks

Once a vertex position is found, tracks with acceptable weights are assigned to the vertex and removed from the track list. Vertices that have at least one beam and one secondary track or vertices which have more than two secondary tracks are defined as good vertices. If a vertex has a beam track, it is labeled as primary; otherwise it is defined as a secondary vertex. The vertex reconstruction process continues in the event until finding a vertex which does not satisfy the good vertex conditions or the number of remaining tracks in the track list is less than two. Figure 4.2 shows the z position distribution of primary vertices for interactions of 120 GeV/c protons on carbon 2%, beryllium, bismuth, and 58 GeV/c proton beam on a carbon 2% target. It can be seen that the vertex z resolution allows to separation of target interactions from scintillator counter interactions.

4.4 Particle Identification

4.4.1 TPC PID

The TPC particle identification is based on mean energy loss of particles per unit pathlength in the TPC. First, energy loss (dE) and uncertainty of energy loss (ddE) are taken from data for each TPC hit. Hits are weighted with the inverse of the uncertainty of the energy losses and pathlengths (dx) are calculated for each hit in a 3σ curve. Then, energy loss per unit pathlegth (dE/dx) is determined. 5% of hits with lower weighted dE/dx and 30% of hits with upper weighted dE/dx are cut from the hit list to determine particle identification. Finally, weighted mean energy loss, which will be represented as dE/dx in the rest of this section, is calculated for a given track; and dE/dx is normalized with minimum dE/dx, which is taken from fitted dE/dx distributions in the course of the run. The second part of the TPC PID package is to determines log-likelihoods for the particle hypothesis of, e, μ, π, K, p, de for a given track using predicted and measured dE/dx values. The functions for

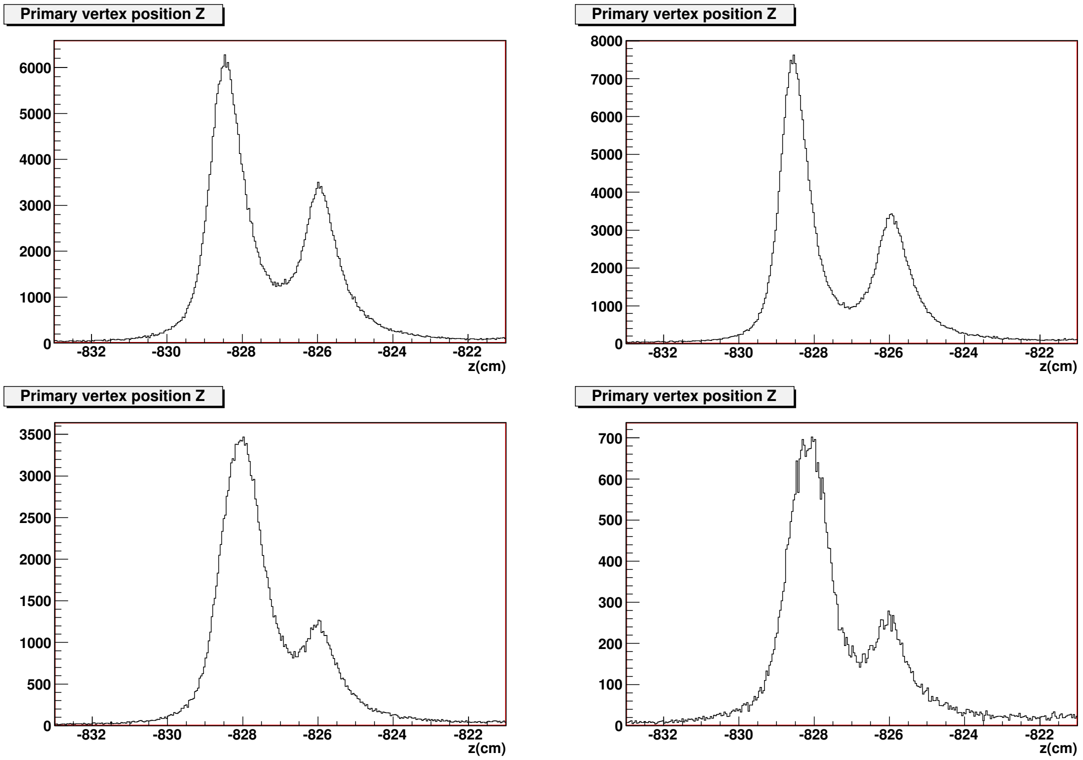

Figure 4.2: Position Z distrubtions of primary vertices. Top left is for 120 GeV/c proton beam on beryllium, top right is from 120 GeV/c proton on bismuth, bottom left and right from proton-carbon interactions for 120 and 58 GeV/c proton beams.

calculating predicted dE/dx values are not strictly Bethe-Bloch functions but are taken from the E910 experiment. After predicted dE/dx values are found for each particle hypothesis, log-likelihoods are set for a given track as below:

$$LL_i = -0.5\frac{(dedx - bb_i)^2}{res_i^2} - 0.5\ln(2\pi res_i^2) \tag{4.4}$$

where $dedx$ is the measured and bb_i is the expected dE/dx for the i^{th} particle hypothesis, res_i is the resolution for the expected dE/dx. In Figure 4.3 the top plot shows normalized dE/dx distributions as a function of total momentum. Solid lines are the Bethe-Bloch functions for each type of particle. The bottom plot shows how to fit dE/dx distribution in each momentum slice to find out the minimum ionization value. The fit function is the combination of the five gaussian functions representing peaks for each particle type.

4.4.2 ToF PID

Particle identification using the ToF counter is based on the largest log-likelihood method. The method takes account of the measured time of flight of a given track between its origin and ToF bars and expected time of flight for each particle hypothesis. Calculation of log-likelihood can be formulated as below

$$LL_i = -0.5\left(\frac{t_{meas} - t_{exp}^i}{t_{res}}\right)^2 - 0.5\ln(2\pi t_{res}^2) \tag{4.5}$$

where t_{meas} is the measured time of flight , t_{exp}^i is the expected time of flight for a certain particle hypothesis, and t_{res} is the time resolution of the bar which is hit for a given track. The measured time of flight and bar resolution are calculated as an average over top and bottom PMTs. The calculation was done for electron, muon, pion, kaon, and proton particle hypotheses. The performance of the particle identification based on mesured velocity can be seen in figure 4.4. It is clearly seen

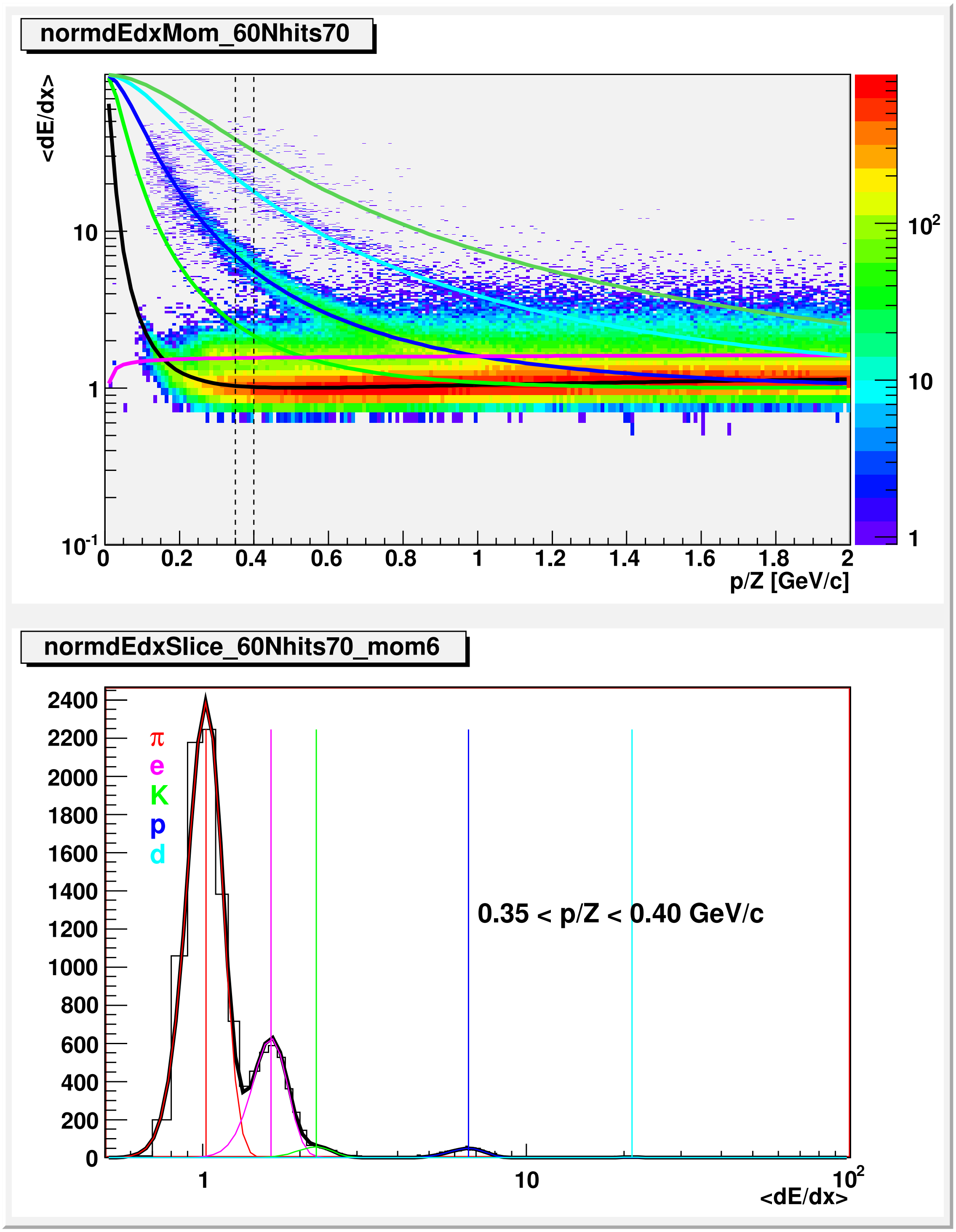

Figure 4.3: The top: dE/dx versus momentum. The bottom: dE/dx distribution in the momentum slice of 0.35 GeV/c to 0.40 GeV/c.

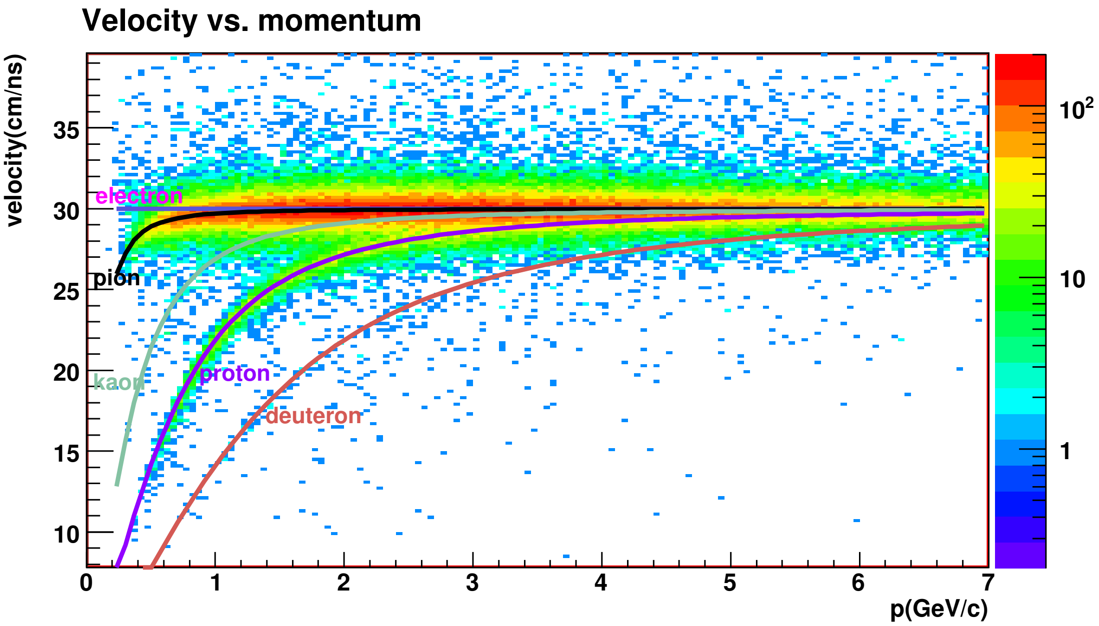

Figure 4.4: Velocity versus momentum for particles emanating from interactions at the target.

that the ToF can seperate pions and protons up to 3 GeV/c.

Another method of particle identification uses the squared mass (m^2) distribution of particles, which is based on the particle velocity. The m^2 is calculated by

$$m^2 = \frac{p^2(1-\beta^2)}{\beta^2} \tag{4.6}$$

where p and β is the momentum and velocity of particle, respectively. The Figure 4.5 shows clearly pion, kaon, and proton peaks in an m^2 distribution.

4.4.3 RICH PID

RICH PID calculates log-likelihoods for electron, muon, pion, kaon, and proton hypotheses for a given track.

The number of photoelectrons produced in a photomultiplier tube per unit

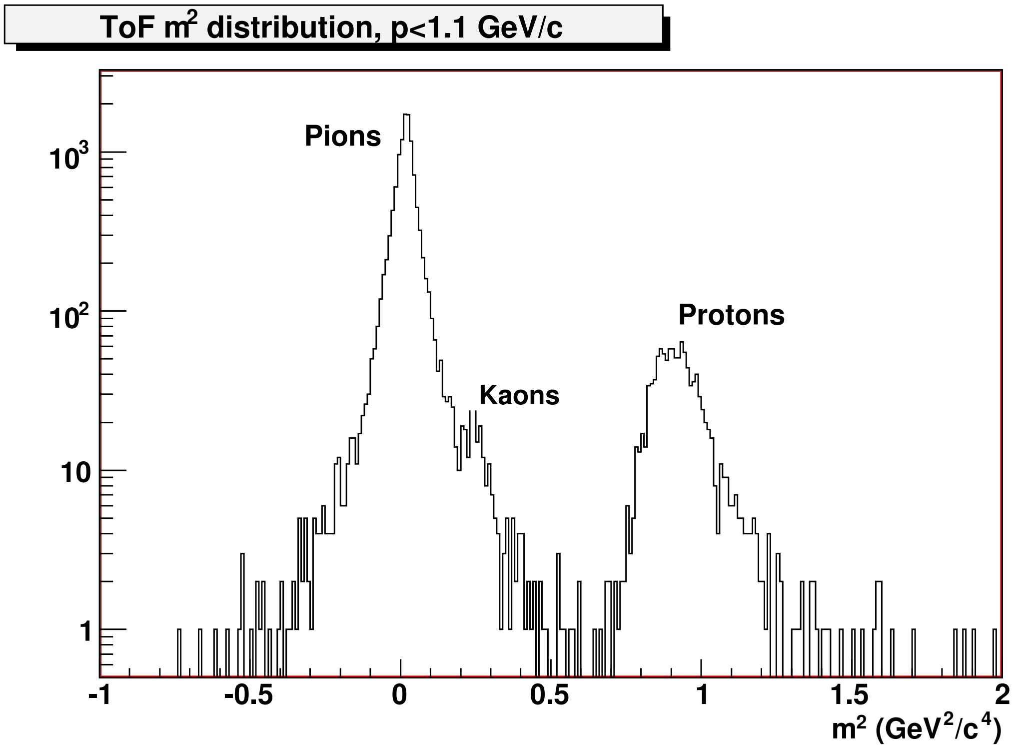

Figure 4.5: Tof m^2 distribution for tracks hitting the ToF wall and with momentum < 1.1 Gev/c.

particle pathlength is given by

$$\frac{dN_e}{dx} = 2\pi\alpha \int (1 - \frac{1}{\beta^2 n^2}) \frac{\epsilon_c(\lambda)}{\lambda^2}\, d\lambda \tag{4.7}$$

where α is the fine structure constant, β is the particle velocity, n is the index of refraction of the medium, and ϵ is the collection efficiency of the photons with the wavelength of λ. The probability that a tube in the RICH PMT base gives a signal if the average number of electrons produced in the tube is N_e can be calculated as

$$\epsilon(\beta) = 1 - exp(-N_e) \tag{4.8}$$

The reason for using this equation is that electron emission in PMTs obeys the Poisson distribution. To calculate likelihoods, first, the ring center is predicted using the momentum and fit parameters of the track. Then, for each particle hypothesis ring radii are determined. The PMTs on a given ring are weighted with the number of observed digits on it for the corresponding track. This way of giving weight eliminates background especially in events with large number of tracks. Finally, the log-likelihoods are calculated as below for a given track using the probability function for giving a signal in each PMT on the rings that correspond to particle hypotheses.

$$logL_j = \begin{cases} \sum_{i=1}^{m} \omega_i log(1 - exp(-N_e^i)(1 - B^i)) & \text{PMT has a hit;} \\ \sum_{i=1}^{m} \omega_i (log(1 - B^i) - N_e^i) & \text{PMT has no hit.} \end{cases} \tag{4.9}$$

where i loops over all PMT digits in a ring that corresponds to the j_{th} particle hypothesis. The detailed explanation of Rich log-likelihood algorithm can be found at [25].

4.5 MC Simulation

The MIPP Monte Carlo simulation package is based on Geant 3.21. Physics processes such as particle production were modeled by FLUKA-2006 and particles were propogated through the spectrometer by Geant creating hits with idealized energy deposition. The hits were stored in ROOT files and converted to digits using MIPP digitization packages.

4.5.1 TPC Digitization

TPC Digitizer collects MC Geant hits; and for each hit, creates digits with ADC values. Digits are defined for some number of voxels which are defined for pad rows, columns, and time buckets. Starting from the hit position, the hit is drifted to the pad plane by 5 us steps with the number of less than 10 to avoid divergence. At the end of each step, hit position is converted to pad row, pad column, and time bucket. Again, at each step, the fractional energy deposition is spread out over pad rows, columns, and time buckets that might be covered by the hit. The number of columns and time buckets in each step are the random Gaussian numbers with the mean and the sigma that are in agreement with real data. The charge is spread out over pad columns and pad rows uniformly but is distributed over time buckets following the Gamma function with the peak at the time bucket found by drifting the hit in a given step. The ADC value for each digit is obtained by scaling the charge by the pad gain factor which is between 0 and 1 and the anode gain factor. Some of all 16 anode regions in the TPC could not hold a high voltage of 1250 V. Therefore, assigning different gains for the anode regions caused MC data to look more like real data. Finally, the pedestal value which is random Gaussian number, is added to the ADC value and digits with ADC above a threshold value were written to the MC ROOT file.

4.5.2 ToF Digitization

The ToF digitizer generates two digits for a given MC hit: one for the top PMT and one for the bottom PMT in the bar that the hit belongs to.

For a given MC hit, first, track that belongs to the hit is found. The track time of flight ($\Delta T01$) between the T01 counter and the position of the associated vertex is calculated. Then, the track is propagated from its position in the bar to the top and bottom PMT faces. Adding the propagation time and $\Delta T01$ to the MC hit time, a hit time that is compatible with data is determined. To make the hit time agree with data, jitter time is added, which is randomly selected gaussian number with 0.1 ns width. Later, time resolution for a given PMT is applied to the time. Finally, the hit time is found after applying slew corrections. The hit ADC value is a randomly selected Landau function with MPV(Most Probable Value) and gain taken from data. Finally, the pedestal value is a randomly selected gaussian number with amplitude and width taken from data.

4.5.3 Čerenkov Digitization

The Čerenkov digitizer takes a MC hit, determines the mirror that the hit belongs to, and calculates the ADC value associated with that mirror. For a given MC hit, the mirror that the Čerenkov light hits are found and is extrapolated to the mirror plane. Ideally, the number of photoelectrons that are created by the hit is calculated. This calculation takes account of waveshifter probabilities for absorbtion and re-emission of the light and PMT efficiencies as a function of wavelength. Then, the ideal number of photoelectrons is scaled by the calibrated response of related mirror. Additionally, the number is scaled by a tuning factor to match to real data. The ADC value is a random Gaussian number. The mean for the Gaussian function is a random Poission number, centered at the tuned number of photoelectrons, scaled by calibration results to convert the number of photoelectrons to an ADC value for a given mirror. The width of the function is the result of noise from the PMT and electronics and depends on the base ADC value. The final ADC value is obtained by adding a pedestal value that is a random Gaussian number with mean and width taken from real data.

4.5.4 Scintillator Digitization

Scintillator digitization loops over MC scintillator hits to calculate the total ADC value for a given event. The ADC value for each hit is a random number from the one mip particle ADC distribution determined from data for each run. It is also multiplied by the particle pathlength over the thickness of the counter. The pedestal value is added to the ADC value as a random Gaussian number with mean and sigma from data. Whether a scintillator trigger is on or not in a MC event is determined by the ADC value being above the threshold ADC value for a given run. The threshold is setup as a random Gaussian number with mean and sigma determined from data run by run. The threshold and the sigma are obtained by fitting ADC distributions for Scintillator triggered events in a given run. The fitting method as follows: First, distribution above Scintillator threshold is fit to an exponential function. Then, the entire histogram is fit to an exponential with a convoluted gaussian function. As a result, the position of the step (error) function and the sigma of the Gaussian function gives the desired values.

4.6 TPC Bad Channel Finding

The 128 front-end cards (sticks) sit in the electronics bay below the padplane. The induced image charges in the pad plane are amplified and digitized by the sticks. Each stick is read out from two pad rows for half of the width of the TPC. Therefore, sticks which is numbered between 0 and 63 read from pad columns 0-59 and sticks numbered between 64 and 127 read from pad columns 60-119. The stick

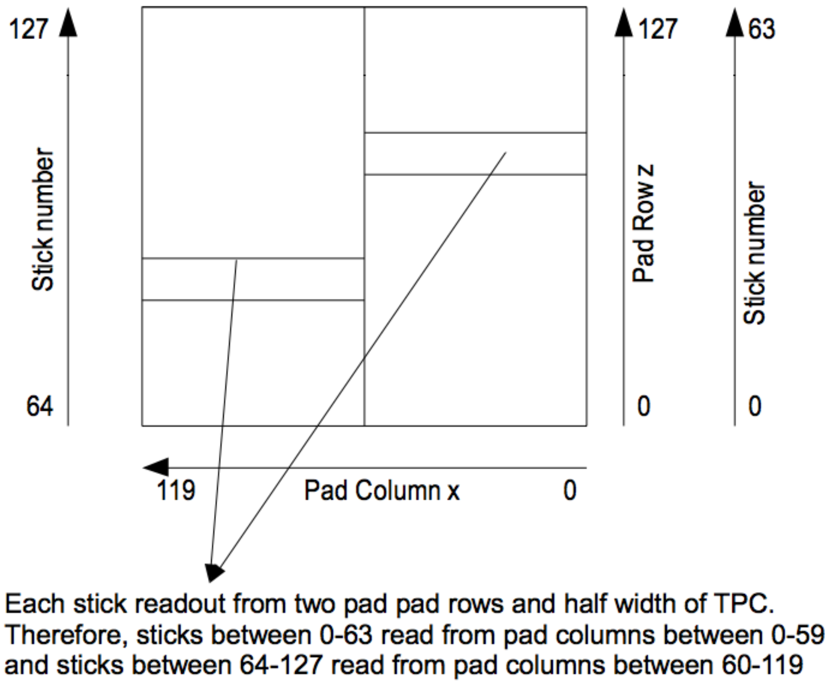

Figure 4.6: TPC stick numbering scheme.

numbering scheme is shown in figure 4.6. The pads which are in the region that a stick covers are also numbered between 0 and 119 for database purposes.

Finding TPC hot and dead channells was done subrun by subrun. To find hot and dead pads, for each target some runs were selected, and the number of raw TPC hits per event as a function of pad plots were created. One of these plots for the carbon target is shown in Figure 4.7. Another type of plot shows the number of hits per event versus the corresponding number of pads. Reading all the plots, it was concluded that pads whose number of hits per event is greater than 40 must be defined as hot, and pads whose number of hits per event is less than 0.001 must be labeled as dead.

Figure **??** shows the number of hot pads in selected runs. The number of hot pads is very high for the run 14243 because of the fun problem in the MIPP hall in May 2005. Otherwise, the number of hot pads is small, less than 50.

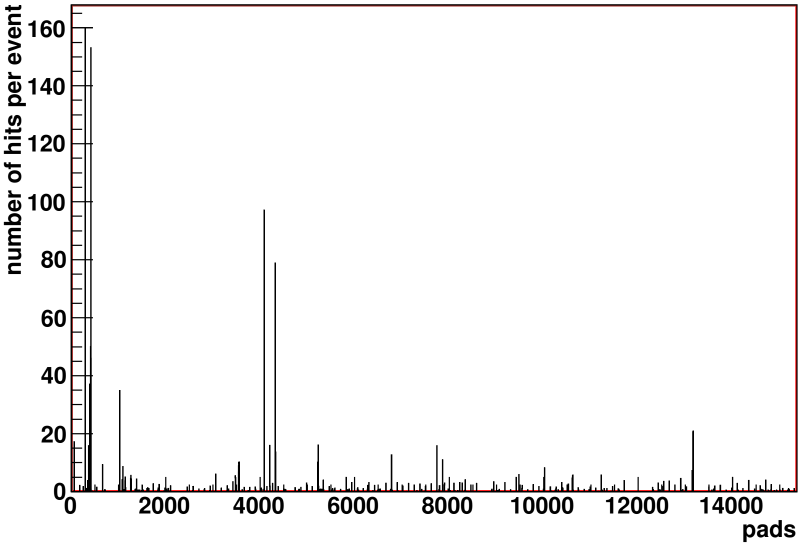

Figure 4.7: Number of TPC hits per event for each pad in a given run.

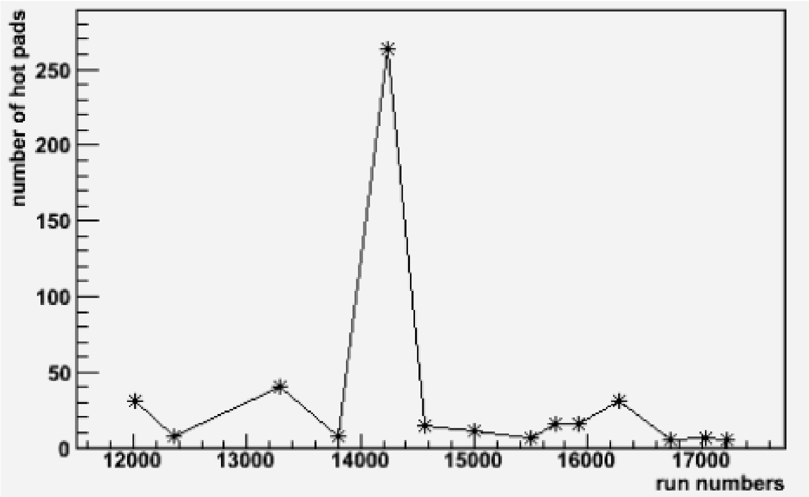

Figure 4.8: Number of hot pads for selected runs that represent different time periods.

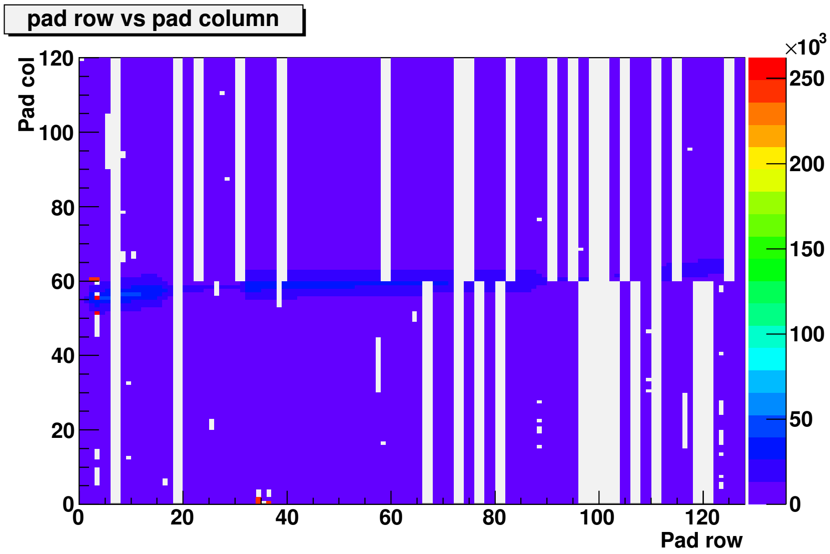

Figure 4.9: TPC hit distrubtion as a function of pad row and pad column after implementing hot and dead pads.

Bad pads were stored in the database subrun by subrun with stick, pad, and status number, which indicates hot or dead pad. Figure 4.9 shows the hit distribution after implementing hot and dead pads to the MC data. White regions indicates there is no hit on those pads because of they are labeled as dead. The pads with red color are clearly identified as hot pads. Finally, hot and dead pads were ignored in the TPC reconstruction package.

CHAPTER 5
DATA ANALYSIS

The presented with this analysis is the measurement of the double differential cross sections of charged pions with longitudinal momentum between 0.24 GeV/c and 1.0 GeV/c and between 30 and 60 GeV/c and with transverse momentum (p_t) that are as large as detector acceptance allows. The cross section results are from the interactions of 120 GeV/c primary proton beam on a 2% interaction length thin carbon target. The details of the data analysis are explained in this chapter.

5.1 Pileup Removal

To avoid more than one incident beam particles in one trigger, pileup events must be removed from data analysis. Pileup removal can be done using the secondary track times and information on the detectors upstream of the target:

- Number of beam tracks;
- Beam track time;
- Three scintillator counters;
- Four beam Čerenkov PMT signals;
- Secondary track times.

The way to select pile up events is to determine the amount of energy (dE/dx) deposited in the TPC using uninteracted beam track events. Since pileup events create multiple peaks in a dE/dx histogram, clean events can be identified by cutting on the dE/dx. The pileup removal for the 120 GeV/c proton beam was done by Andrey Lebedev and the details can be found at [19]. In the analysis, events that have dE/dx less than 2 and greater than 3 were identified as clean events and pile-up candidates, respectively. The cuts to remove pileup events for 120 GeV/c proton beam are:

1. The number of beam tracks more than 1;

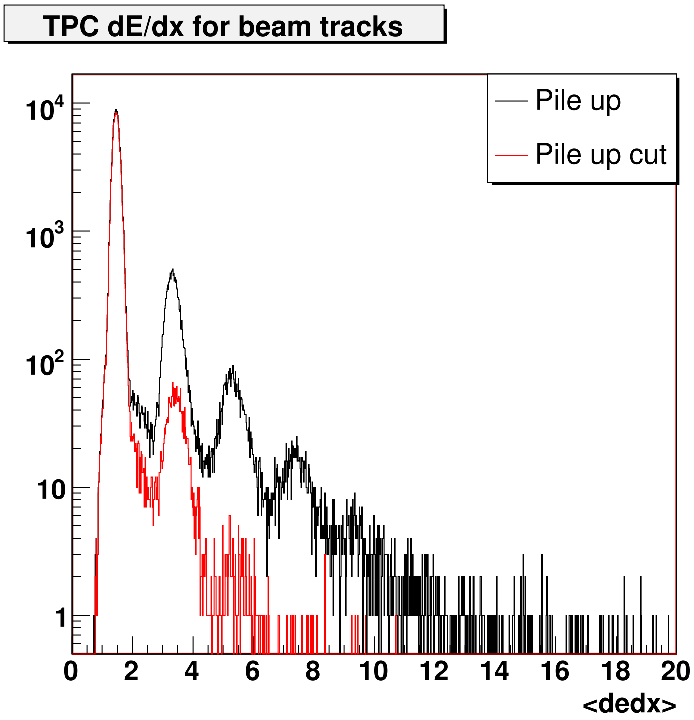

Figure 5.1: dE/dx with or without pile up removal.

2. The average charge of beamline scintillator counters is greater than 1.8;
3. The beam track time is outside of the 5 to 20 ns window;
4. Large (greater than 1 ns) time difference of signals in beam scintillator counters;
5. The average charge of beam Cherenkov counters is larger than 330 in ADC units;
6. A TDC hit in the outer PMT of either beam Cherenkov counter (none are expected);
7. The TDC time of the inner PMT of the upstream beam Cherenkov counter is less than 800 or greater than 1040;
8. The TDC time of the inner PMT of the downstream beam Čerenkov counter is outside of the 700 to 950 window.

The figure 5.1 shows how most of the extra peaks are removed in a dE/dx distribution of the uninteracted beam tracks when pile up cuts are applied.

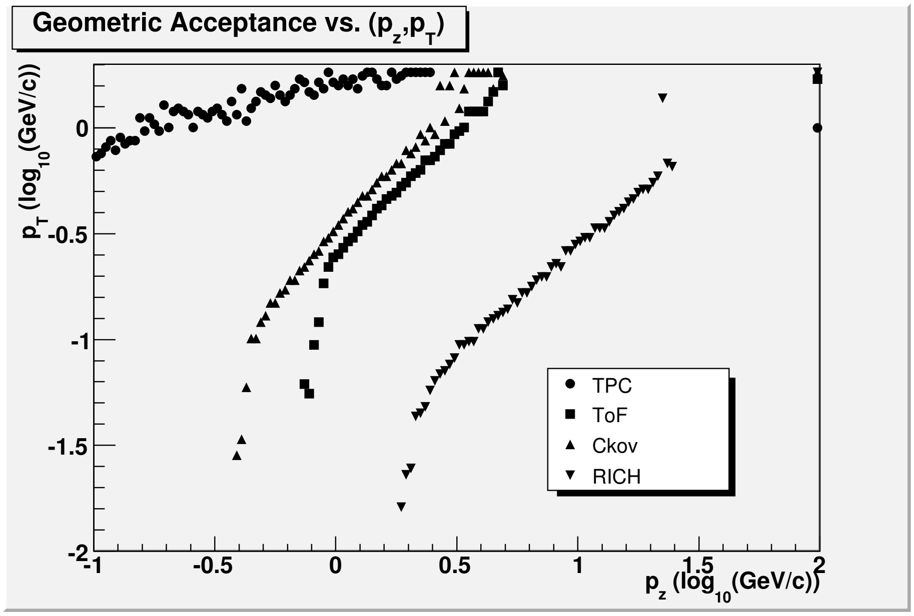

Figure 5.2: p_t bounduries as a function of p_z where acceptance goes above 50%.

5.2 Geometric Acceptance

Geometric acceptance were calculated to select longitudinal and transverse momentum bins for different particle identification detectors. Monte Carlo root files were used and tracks are defined as accepted if they satisfy the conditions below:

- Track pathlength in TPC must be 10 cm
- It is required one ToF hit
- One Ckov hit is required and track must go through front window of Ckov
- One RICH hit and track must reach front window of the RICH

The Figure 5.2 shows p_t boundaries as a function of p_z at which acceptance starts to go above 50%.

Table 5.1: Selected momentum bins

bin	min p_z	max p_z	min p_t	max p_t	bin	min p_z	max p_z	min p_t	max p_t
(0,1)	0.24	0.32	0.10	0.20	(3,4)	0.60	0.80	0.40	0.50
(0,2)	0.24	0.32	0.20	0.30	(3,5)	0.60	0.80	0.50	0.60
(0,3)	0.24	0.32	0.30	0.40	(3,6)	0.60	0.80	0.60	1.60
(1,0)	0.32	0.42	0.00	0.10	(4,0)	0.80	1.00	0.00	0.10
(1,1)	0.32	0.42	0.10	0.20	(4,1)	0.80	1.00	0.10	0.20
(1,2)	0.32	0.42	0.20	0.30	(4,2)	0.80	1.0	0.20	0.30
(1,3)	0.32	0.42	0.30	1.30	(4,3)	0.80	1.0	0.30	0.40
(2,0)	0.42	0.60	0.00	0.10	(4,4)	0.80	1.0	0.40	0.50
(2,1)	0.42	0.60	0.10	0.20	(4,5)	0.80	1.0	0.50	1.70
(2,2)	0.42	0.60	0.20	0.30	(5,0)	30.0	42.0	0.00	0.20
(2,3)	0.42	0.60	0.30	0.40	(5,1)	30.0	42.0	0.20	0.40
(2,4)	0.42	0.60	0.40	0.50	(5,2)	30.0	42.0	0.40	0.60
(2,5)	0.42	0.60	0.50	0.60	(5,3)	30.0	42.0	0.60	1.20
(2,6)	0.42	0.60	0.60	1.65	(6,0)	42.0	60.0	0.00	0.30
(3,0)	0.60	0.80	0.00	0.10	(6,1)	42.0	60.0	0.30	0.40
(3,1)	0.60	0.80	0.10	0.20	(6,2)	42.0	60.0	0.40	0.60
(3,2)	0.60	0.80	0.20	0.30	(6,3)	42.0	60.0	0.60	1.20

5.3 Bin Selection

To calculate double differential cross sections, we selected eight longitudinal momentum (p_z) bins and a different number of p_t bins within the geometric acceptance. When selecting bin sizes, it was taken account that the bins must be sufficiently large to obtain enough statistics and momentum resolution which is 5.5% at most must not mix the bins. Also, track reconstruction efficiency are above at least 70% in selected bins. The bin boundaries are shown in table 5.1.

5.4 Primary Vertex Selection and Empty Target Subtraction

In this analysis, events that were triggered by the scintillator counter were selected. This is because the performance of the scintillator is known better than the iDC and also the iDC had some inefficiency problems as explained in section

3.4. Additional constraints on the primary vertex is the x and y position of the events at target Z. Primary vertex x and y position relative to the target center is shown in figure 5.3. It is seen that the beam is focused at the coordinates of 0.037 cm in x and 0.51 cm in y. It was restricted that the radial distance of the events relative to the target center must be within 1.5 cm to ensure all events come from target interactions. Since target-out data will have more interactions in the scintillator counter compared to the target-in data, the target-out data must be scaled before subtraction from the target-in data. To do that, primary vertex z distributions were plotted for target-out and target-in data including target and scintillator interactions. The shape of the target-out data follows a Gaussian distribution with exponential tails on both sides plus a constant background. The target-out data were fitted to that function. Then, target-in data was fit to the combinations of the two Gaussian with exponential tails: One represent the target peak and one represents the scintillator peak. The integrals of the fit functions indicated that the target-out data must be scaled by 0.776 before it is subtracted. The figure 5.4 shows the fit results.

The fit function is formulated as below

$$f(z) = \begin{cases} Aexp\left(-\frac{1}{2}\left(\frac{z-z_{mean}}{\sigma_z}\right)^2\right) + const. & \text{if } |z-z_{mean}| < \sigma_{cut}\sigma_z; \\ Aexp\left(\frac{1}{2}\sigma_{cut}^2 - \frac{|z-z_{mean}|}{\sigma_z}\sigma_{cut}\right) + const. & \text{if } |z-z_{mean}| \geq \sigma_{cut}\sigma_z. \end{cases} \tag{5.1}$$

where σ_{cut} determines how many σ to the right and left the function becomes exponential, z_{mean} is mean number of the Gaussian function.

5.5 Interaction Trigger Efficiency

Scintillator trigger efficiency was calculated by using a MC simulation. It was done by determining how often the trigger was fired when there is a target-like interaction in a given event. The efficiency was calculated as a function of

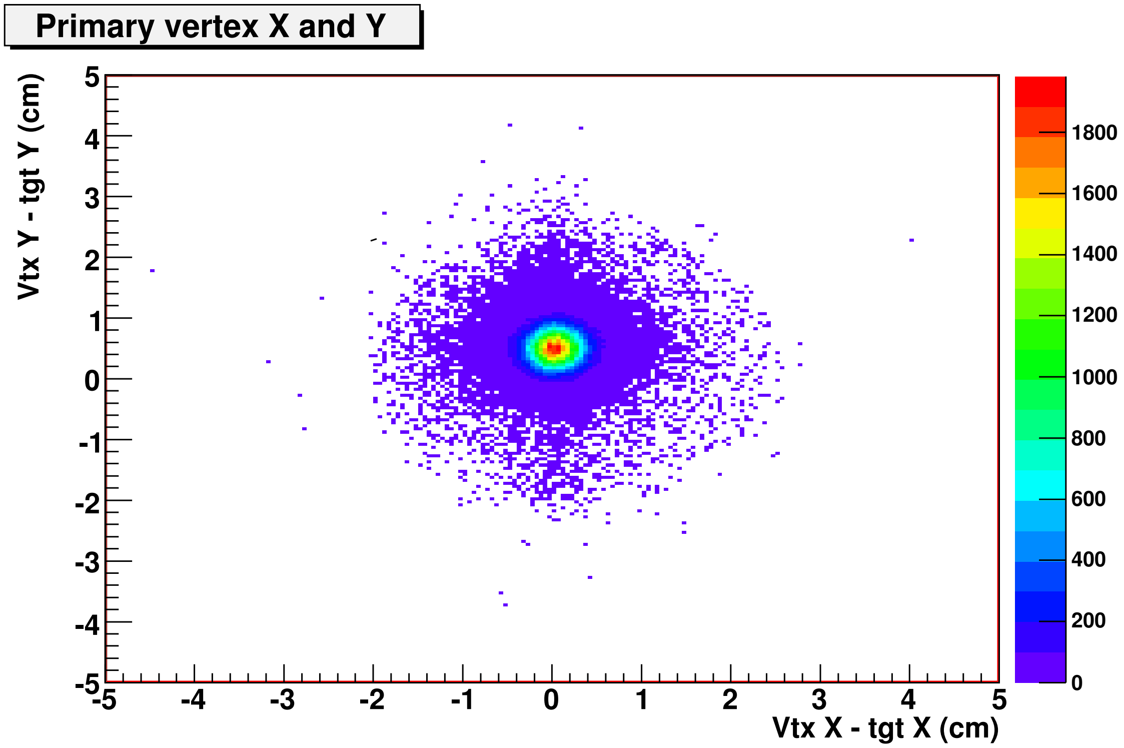

Figure 5.3: Primary vertex X and Y position distribution at target.

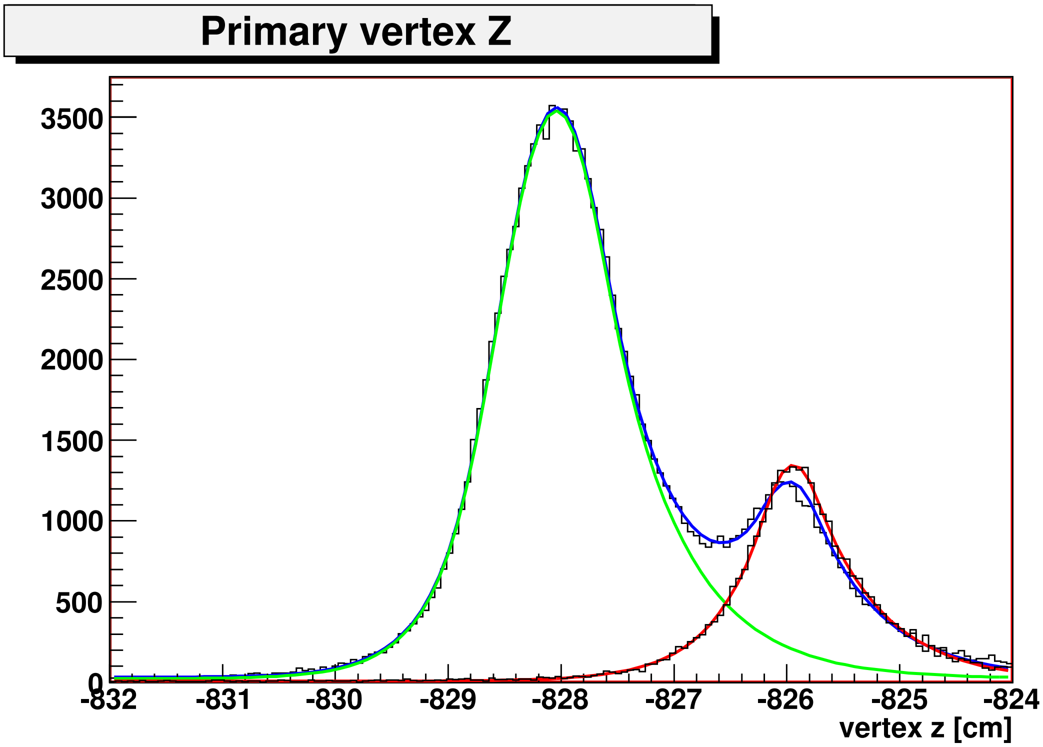

Figure 5.4: Primary Vertex Z distribution

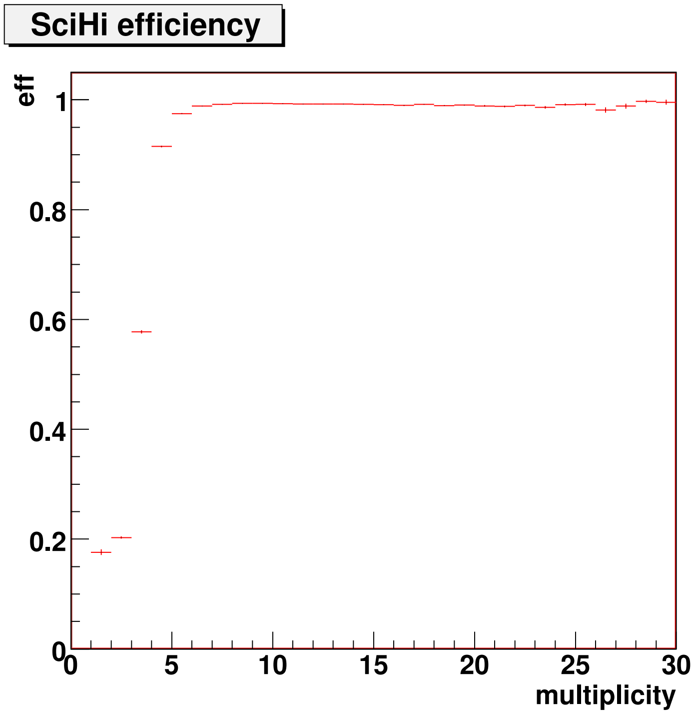

Figure 5.5: Scintillator trigger efficiency as a function of track multiplicity.

the number of tracks passing through the counter in an event. Therefore, in cross section calculation, the efficiency numbers were applied event by event. Figure 5.5 shows the efficiencies.

5.6 Beam Flux Calculation

Beam flux can be determined in two different ways. One is to sum prescale numbers for each beam triggered event in the data set. It is because beam triggered events need a certain number of raw beam pid trigger signals to be read out. For the 120 GeV/c proton carbon data that was used in this analysis, proton beam pid events were prescaled with 500. The figure 5.6 shows prescaled trigger bits that caused to read out. 17,974 proton beam events caused the beam flux to be calculated as 9,004,974.

The second method is to read raw trigger scalers. In each spill, the number raw

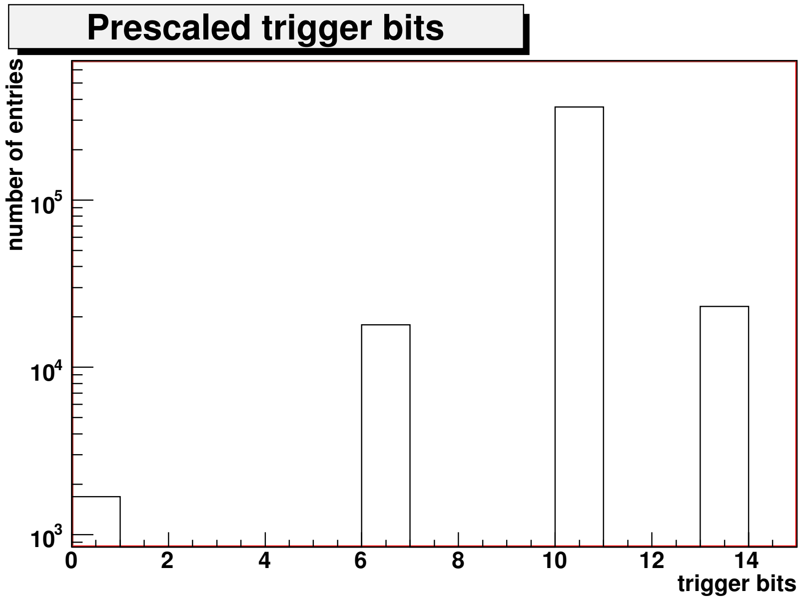

Figure 5.6: Prescaled trigger bits. Trigger bits 0 and 6 are beam id and beam pid triggers that do not require an interaction trigger. Trigger bit 10 requires an interaction trigger and is not prescaled in the case of our analysis. 13 is the inter-spill calibration pulser trigger.

trigger signals are recorded. Basically, two types of scalers are set: gated and un-gated. Un-gated scalers count all trigger signals, but gated scalers are used when the detectors are not read out (live-time). Therefore, reading gated raw proton beam pid scaler for each spill would give required beam flux. Since scalers in some runs did not give accurate numbers due to unknown causes, we use the beam flux calculated from prescalers in this analysis.

Since pile up events are removed from the data set, we must reduce beam flux by the appropriate factor. This factor is obtained by taking the ratio of the pile up events to the total number of events used in the analysis. The factor for our data set was found to be 0.732.

5.7 Terminology of Cross Section

Cross section represents the probability of an interaction between a beam particle and a target. The unit of the cross section is the area that defines a region around a scattering center within that an interaction may occur.

Exclusive cross section means the probability of observing an exclusive final state, e.g. $pp \rightarrow \pi^+ n$. Inclusive cross section determines the interaction rate of some final state particles, e.g. $pp \rightarrow \pi^+ X$.

The unit of the cross section is the barn ($1b = 10^{-28} m^2$). Usually, differential cross section is measured as a function of solid angle $d\Omega$. If beam or target is not polarized, cross section depends only polar angle θ but not azimuthal angle ϕ.

Differential cross section from experimental data as a function of solid angle $d\Omega$ is measured as

$$\frac{d\sigma}{d\Omega} = \frac{dN_{int}}{N_{beam} \cdot n_{tgt} \cdot d\Omega} \tag{5.2}$$

where

- dN_{int} is the number of interactions with a final state particle goes into a solid angle $d\Omega$

- N_{beam} is the number of incident beam particles

- $n_{tgt} = \frac{N_A}{V_{mol}} \cdot L_{tgt}$ is the areal target density, number of target particles per unit area (N_A is Avagadro's number, V_{mol} is the molar volume, molar mass divided by density, and L_{tgt} is the target length along the beam direction) .

The detailed explanation of cross section measurements in the MIPP is documented at [22].

5.8 The formula for cross section

The double differential cross section as a function of longitudinal and transverse momentum that a final state particle goes into is calculated as below

$$\frac{d^2\sigma}{dp_z dp_t}(p_z, p_t) = \frac{A}{N_A \rho} \frac{1}{a(p_z, p_t)} \frac{N_{tgt}(p_z, p_t) - N_{empty}(p_z, p_t)}{N_b(\Delta p_z)(\Delta p_t)} \tag{5.3}$$

where

- A is the atomic mass of the target (A=12.0107 g for carbon);

- N_A is the Avagadro number;

- ρ is the areal density of the target;

-a is the acceptance and efficiency of the detectors;

- N_{tgt} and N_{empty} are the number of pions reconstructed in momentum and angle bins for target-in and target-out data, respectively;

- N_b is the number of beam (protons) particles on the target;

- Δp_z and Δp_t are the longitudinal and transverse momentum bin sizes.

5.9 Likelihood Weighted Particle Identification

In this analysis, particles with longitudinal momentum between 0.24 and 1.0 GeV/c are identified using the TPC detector and particles with longitudinal momentum between 30.0 and 60.0 GeV/c are identified by the RICH detector. For a given track, a weight is determined for each particle hypothesis based on the likelihood values. The larger likelihood have larger weight. In the analysis, the pion weight for each particle is filled into the appropriate momentum bin. For a given particle hypothesis, the weight is defined as below:

$$wt_i = \frac{exp(LL_i)}{\sum_i exp(LL_i)} \tag{5.4}$$

where LL_i is the likelihood for i^{th} particle.

For identification of particles with p_z up to 1.0 GeV/c, iterative weighting method was used. Before starting iteration, weights are calculated using the log-likelihood values. Using these weights, histograms are created for the particle hypothesis of electron, pion, kaon, proton, and the sum of all weights as a function of inverse of the square of the total momentum. The histograms are fitted to the function of exponential of the polynomial as shown below. The fit functions belong to particle types are divided to that belong to the sum of all weights. These are called prior probabilities for particle species. Once priors are determined, they contribute to the weights calculation. At each iteration, with the previous priors, new weights are constructed and new priors are determined. Finally, at a certain iteration, the fit functions and likelihood weighted momentum distributions converge and priors become stable. The likelihood weighted momentum distribution of pions at the first and 19^{th} iteration and pion prior probabilities are shown in Figure 5.7. The same histograms for MC are shown in Figure 5.8. It is seen that pion prior probabilities increase with the iterations in the momentum of close to 1 GeV/c. It is because in that momentum region particle dE/dx bands merge but determining priors with the fit functions at each iteration helps to reach correct particle weights. Finally, after 19^{th} iteration pion prior probabilities for MC and data were used to calculate weights in the interested analysis. As shown in Figure 5.9 the priors agree with each other well.

$$\begin{aligned} &x = ln(1/p^2); \\ &f = exp(a + b * x + c * x^2 + d * x^4). \end{aligned} \tag{5.5}$$

5.10 Monte Carlo Corrections to Data

5.10.1 Purity Correction

The purpose of the purity correction is to find the number of pions (pion weights) that belongs to true pions. To do that, for each reconstructed particle in

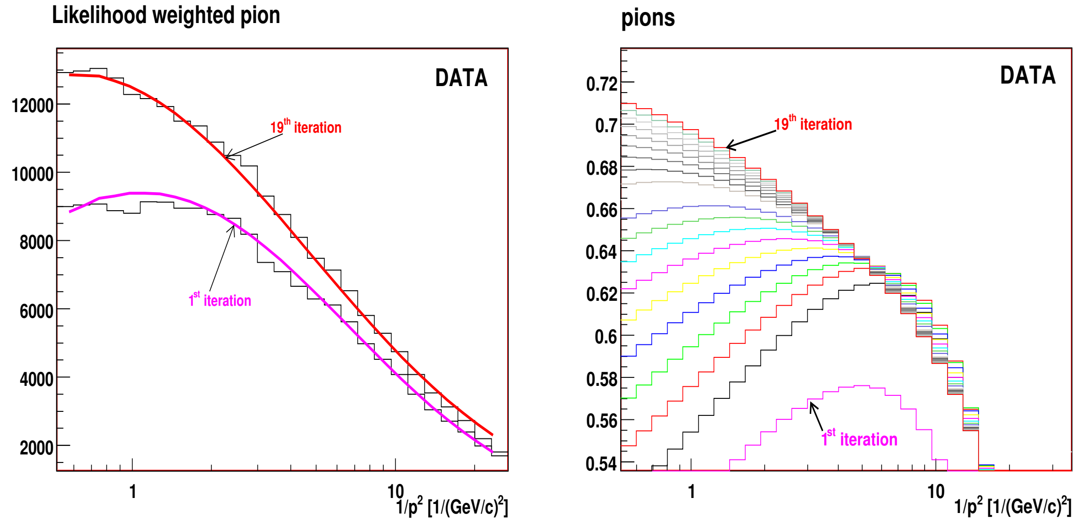

Figure 5.7: On the left likelihood weighted momentum distribution of pions. Solid lines are the fit functions. On the right prior probabilities for pions.

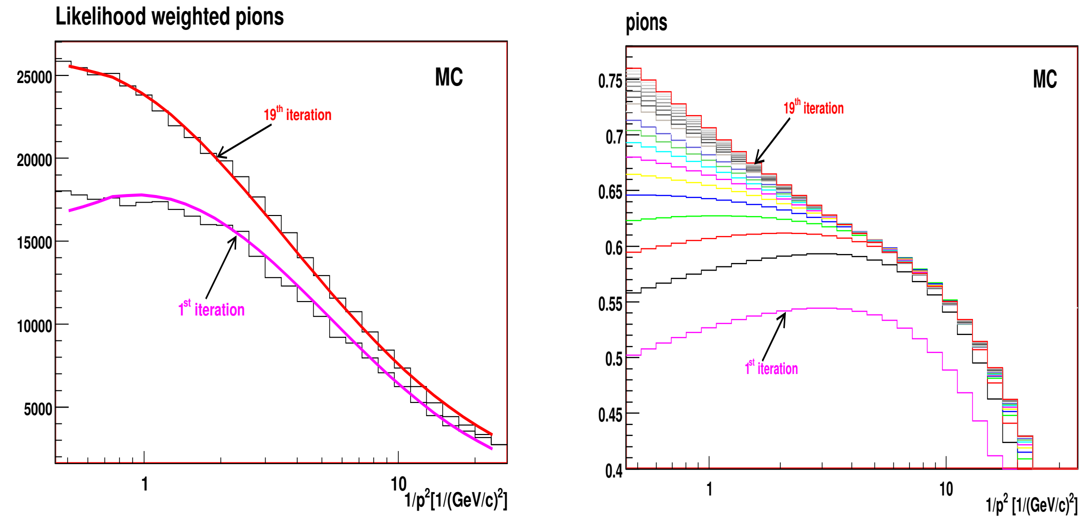

Figure 5.8: On the left likelihood weighted momentum distribution of pions and on the right prior probabilities for pions.

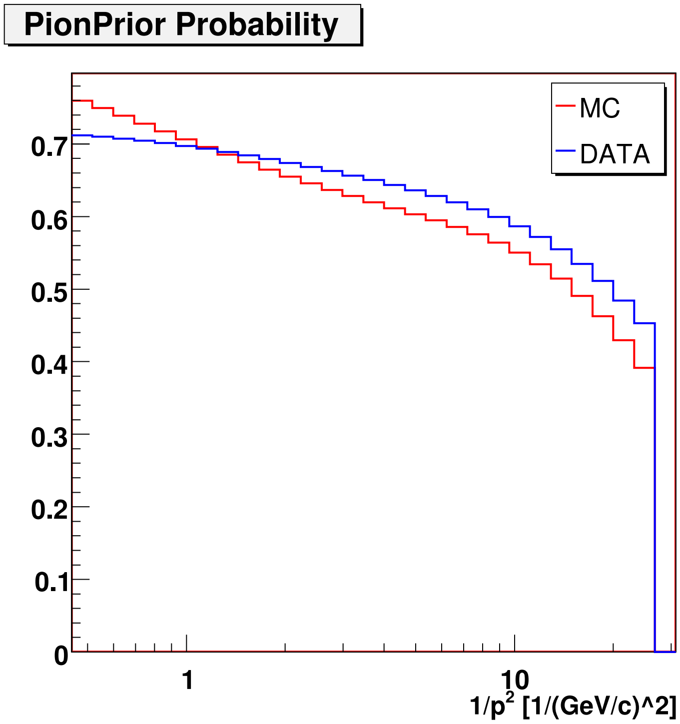

Figure 5.9: Pion prior probabilities after 19^{th} iteration for MC and Data .

MC, the sum of pion weights were determined in reconstructed momentum bins. Then, the sum of pion weights that is from true pions in the same bins were found. The ratio of the bin contents in the histograms provided the purities for the momentum bins. The Figure 5.10 shows the purity numbers.

5.10.2 Momentum Correction

The MIPP has particle momentum resolution 2% at low momentum and up to 5.5% at high momentum. Therefore, it is necessary to correct mixing between momentum bins. For that, a migration matrix were created for positive and negative particles using MC Truth and Reco information. The histograms shown in figure 5.11 and 5.12 give the probability that the reconstructed bin falls into a true momentum bin. It is seen that on average 70 %, reconstructed bins finds true bins. These factors were applied to the data to obtain the correct number of particles in

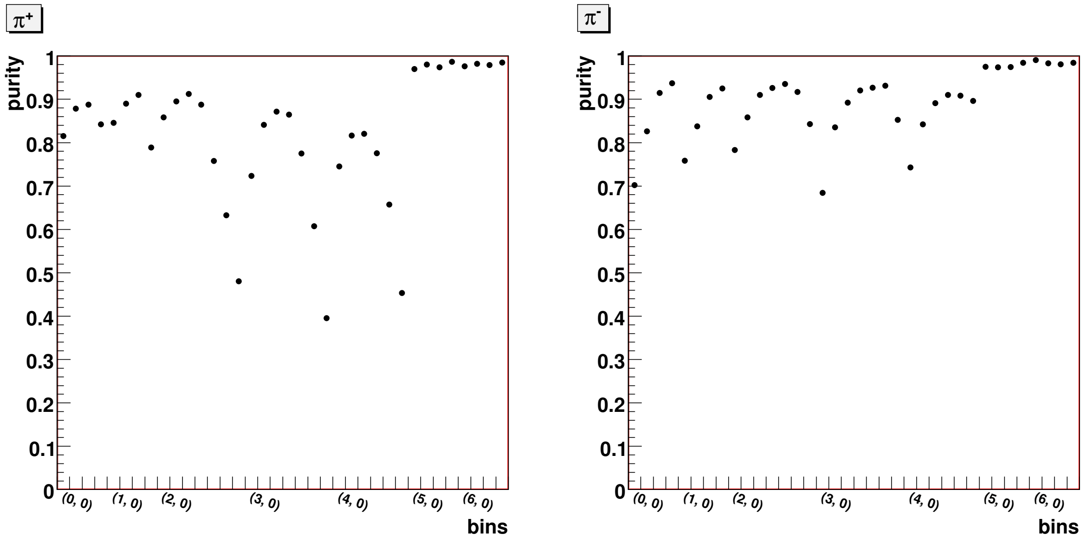

Figure 5.10: The numbers for purity correction for pions.

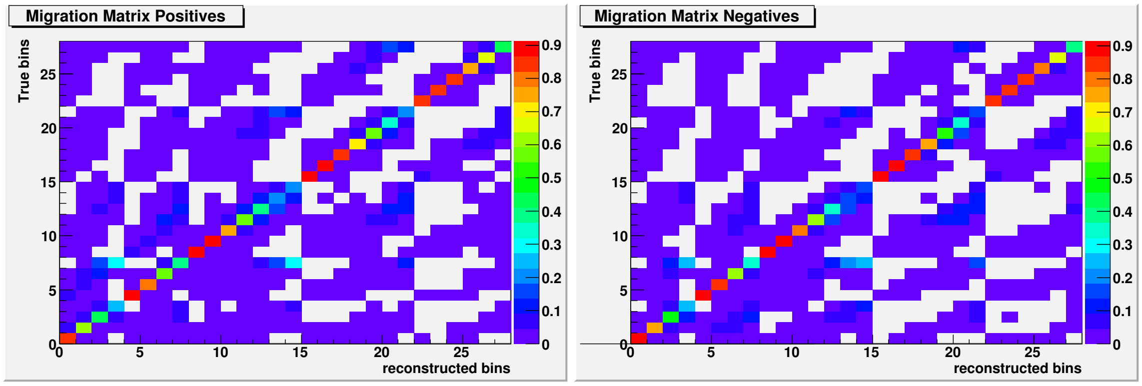

Figure 5.11: On the x axis reconstructed bins, y axis the probability that reconstructed bin falls into true momentum bin for the bins with p_z up to 1.0 GeV/c.

selected bins. The purities are very high in the bins with longitudinal momentum above 30 GeV/c, close to 100%. For the bins with momentum less than 1 GeV/c, at larger angles, the purities decrease below 50%.

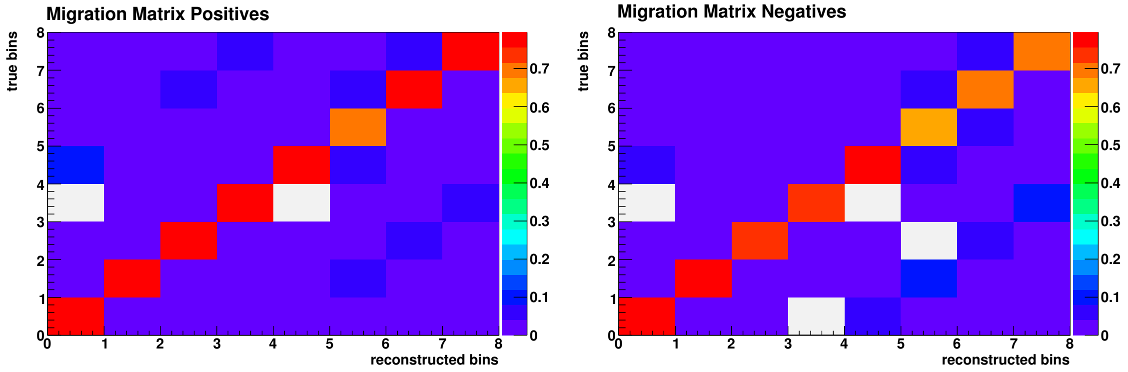

Figure 5.12: On the x axis reconstructed bins, y axis the probability that reconstructed bin falls into true momentum bin for bins with p_z between 30.0 and 60.0 GeV/c.

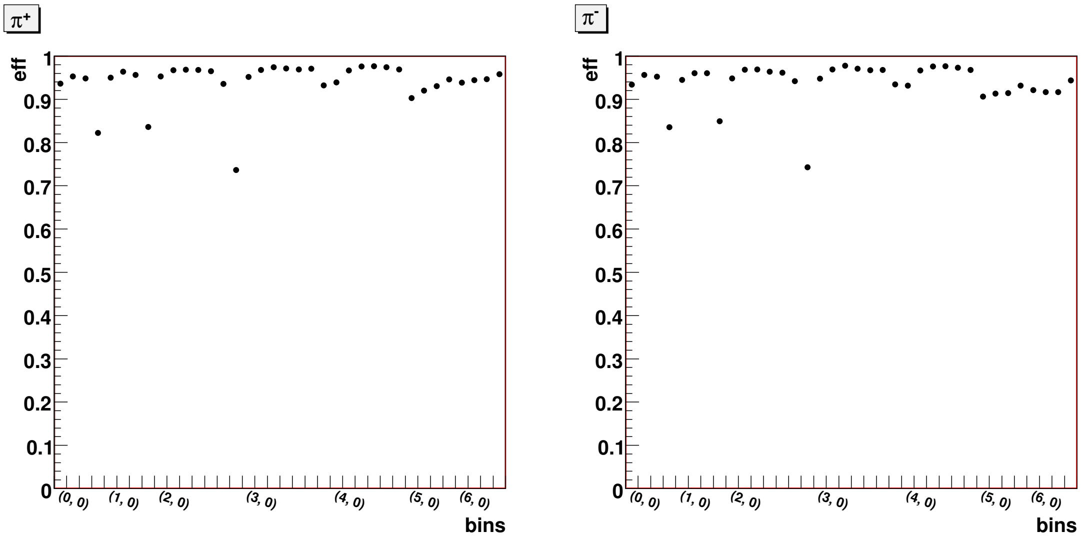

Figure 5.13: Track reconstruction efficiencies in true momentum bins.

5.10.3 Track Reconstruction Efficiency

Track reconstruction efficiency was done by looping over MC true tracks to find how often true tracks are reconstructed by the MIPP reconstruction package in true momentum bins. The efficiencies are around 95% in most of the bins except at the largest transverse momentum bin with longitudinal momentum less than 1.0 GeV/c.

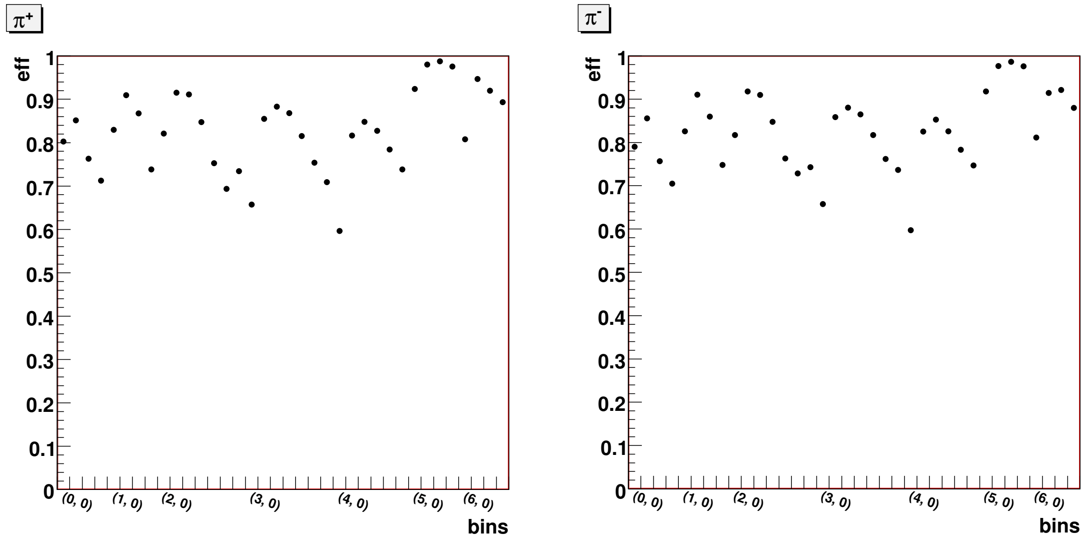

Figure 5.14: Pid efficiencies for pions. These corrections were applied to data bin by bin.

5.10.4 Particle Identification Efficiency

PID efficiency was done by looping over MC truth tracks and accumulating pion pid weights when the track is a true pion. Then, the ratio of the sum of the pion weights to the number true pions in each true momentum bins gives the pion identification efficiency.The efficiencies for positive and negative pions are shown in figure 5.14. It is seen that, in the same longitudinal momentum bin, at larger p_t's, efficiencies start to decrease.

5.11 Systematic Errors

5.11.1 Systematic Error from Primary Vertex Cut

As explained in section 5.4, the primary vertex z for events were restricted to have events only from interactions in the target. However, there may be some interactions whose vertex z were reconstructed away from the target region. To

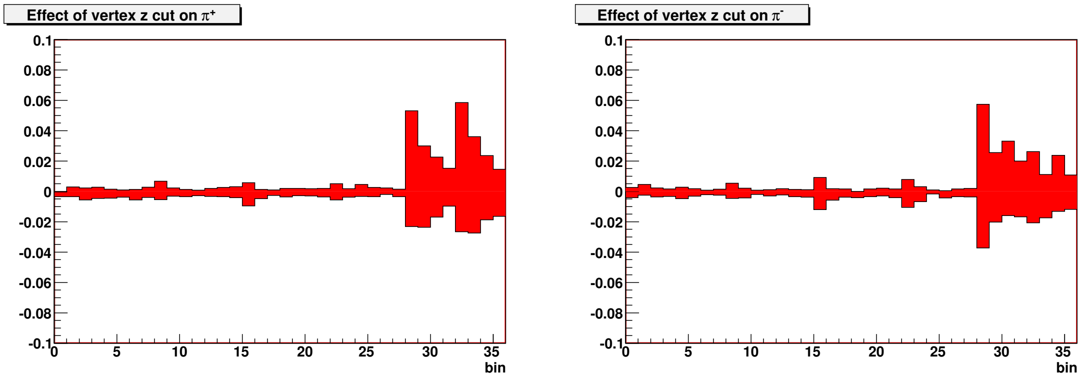

Figure 5.15: The effect of vertex z cut on cross section values.

investigate this situation, we opened larger and narrower vertex z window ($-840 < V_z < -820$ and $-830 < V_z < -825$). It was seen that the effect of these changes on the cross sections very small in the bins with p_z less than 1.0 GeV/c ,but could be up to 6% in higher momentum bins for π^+ and π^- as shown in figure 5.15.

5.11.2 Systematic Error from Interaction Trigger Efficiency

Even scintillator counter was well modeled in Monte Carlo simulation and trigger efficiencies were calculated using MC, the efficiencies were increased and decreased 10% and uncertainty on the cross section values was calculated as an up and down error for each bin. The effect of uncertainty of the interaction trigger efficiency on the cross section is shown in Figure 5.19. It can be seen that the effect on the cross section values does not exceed 4% even in the higher longitudinal momentum bins with lower statistics.

5.11.3 Systematic Error from Empty Target Subtraction

Systematic error from empty target subtraction was studied simply by changing the empty target scaling factor 5% and see the changes on the cross sections. The effect is very small around 0.5% as shown in Figure 5.17.

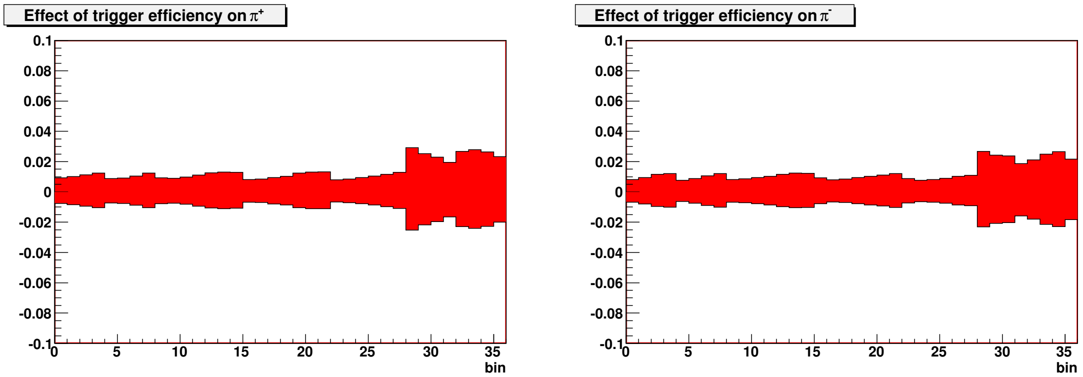

Figure 5.16: The effect of trigger efficiency uncertainties on cross section values.

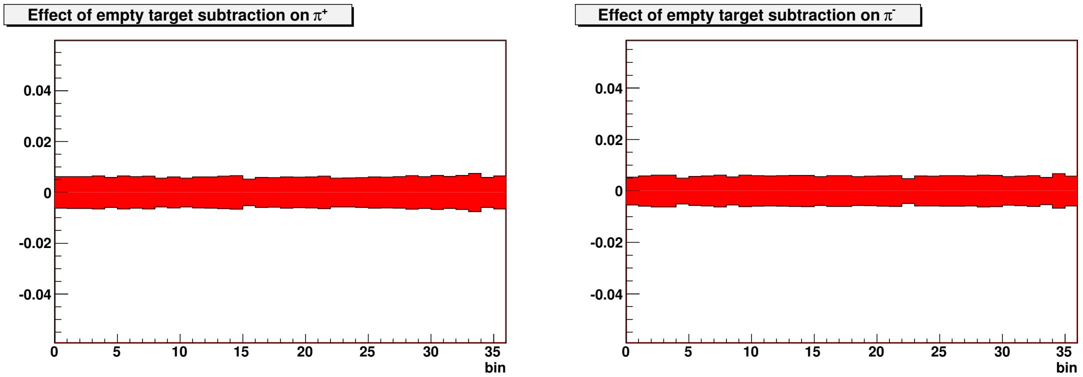

Figure 5.17: The effect of uncertainties of empty target scaling factor on cross section values.

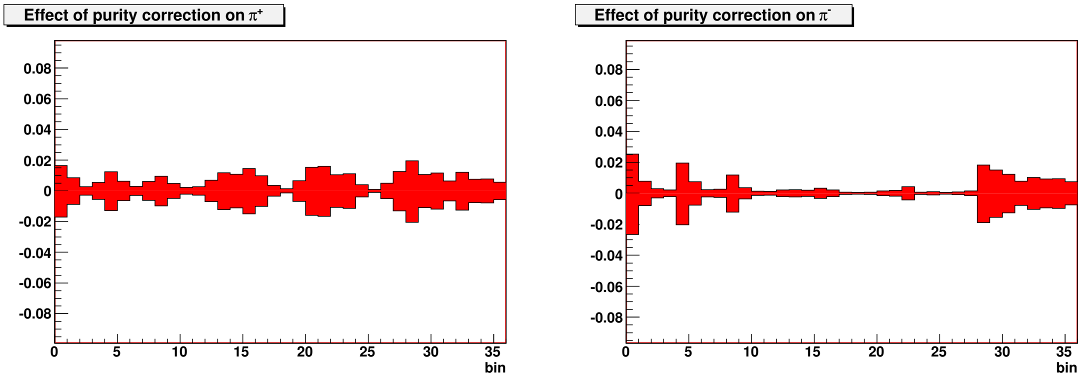

Figure 5.18: The effect of purity correction on cross section values.

5.11.4 Systematic Error from Purity Correction

One of the sources of the uncertainty on the purity correction is the difference between data and MC simulation for the number of pions relative to the other particles. The ratio of the sum of the pion weights to the total weights were determined in both MC and data for each momentum bin. Then, new purities were calculated using the differences of the ratios between MC and data as below and cross sections were recalculated with the new purities.

$$P' = (1 + dP) * P - dP \tag{5.6}$$

$$P' = (1 - dP) * P + dP \tag{5.7}$$

where dP is the difference of the pion weight ratio between data and MC as a percentage. The effect is very small less than 2%.

5.11.5 Systematic Error from PID efficiency

Since dE/dx distribution can be different between data and MC even for true pions, the sum of pion weights with greater than 0.5 were compared between data and MC by the normalized entries bin by bin. The new pid efficiencies were

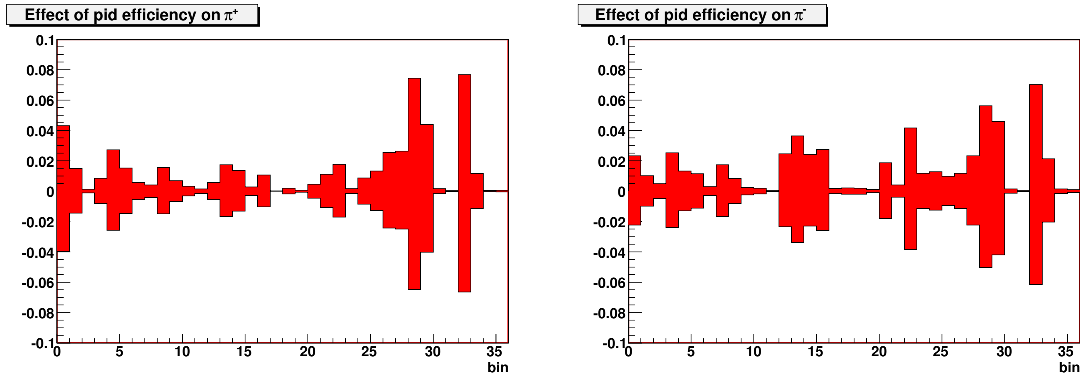

Figure 5.19: The effect of uncertainties of particle identification efficiencies on cross section values.

calculated using the differences as a percentage. The results are shown in Figure 5.19. The effect is small in most of the bins but can be up to 8 % in the high momentum bins.

5.12 Validation of the Analysis

In order to confirm proper operation of the detector and to validate analysis techniques it is useful to reproduce well known results. For this purpose two studies were carried out. For the first study interactions of proton beam on the liquid hydrogen target were analyzed for track multiplicity and the KNO scaling behavior was compared to published results. The largest difficulty in this study was the clean separation of elastic scattering events and events with un-interacted beam tracks from inelastic events. This resulted in differences in the observed yield for multiplicities below three from KNO expectation. As data on liquid hydrogen was not taken at 120 GeV/c this study was performed using data at 58 GeV/c and 85 GeV/c. We could then use the cuts developed for the KNO analysis to obtain a total inelastic cross section for p-p interactions. The results are not presented here, but agree with published values. The second study determined the total cross section of proton carbon interactions at 120 GeV/c. This study used cuts very similar to the cuts developed in the first study. Results for the total cross section seem reasonable, but depend on the acceptance from MC which in turn relies on a correct cross section model in the event generator. The total cross section is in reasonable agreement with extrapolations from published results of other experiments.

CHAPTER 6
RESULTS

Following the analysis technique described in the previous chapter we obtain double differential cross sections for the interaction of 120 GeV/c protons on a thin carbon target for the reactions $pC \rightarrow \pi^+X$ and $pC \rightarrow \pi^-X$ as a function of longitudinal and transverse momentum of the produced pion. The results are shown for 28 bins of momentum up to 1 GeV/c and 8 bins of momentum between 30 and 60 GeV/c. The bin boundaries are shown in table 5.1. The cross sections are shown in the histograms as a function of p_t for each p_z bin in Figures 6.1 and 6.2. The results are also in tables at 6.1 and 6.2. The errors in the histograms are the total errors and were calculated as a quadratic summation of the individual errors. The systematic error from beam flux calculation is not shown in the tables but it is taken as an overall 5%. It is because beam flux from using prescale numbers of beam pid triggers are different 4% from counting end of spill trigger scalers.

The shape of the cross section distributions follows the expected pattern of cross sections at a given momentum falling with increasing p_t. The statistical errors are small due to high statistics that was enabled by the TPC technology in the MIPP experiment. Many possible sources of systematic error were studied. It was found that the leading systematic uncertainties are due to primary vertex z position cut, beam flux, trigger efficiency, empty target subtraction, and MC acceptance. Other sources of systematic error were deemed negligible by comparison. Errors shown in the plots are total errors that were calculated as quadratic summation of individual errors.

In summary, we present differential cross sections for p-C interactions using MIPP data. Several improvements to the present analysis are possible. The most significant of these is the inclusion of momenta between 1 and 30 GeV/c.

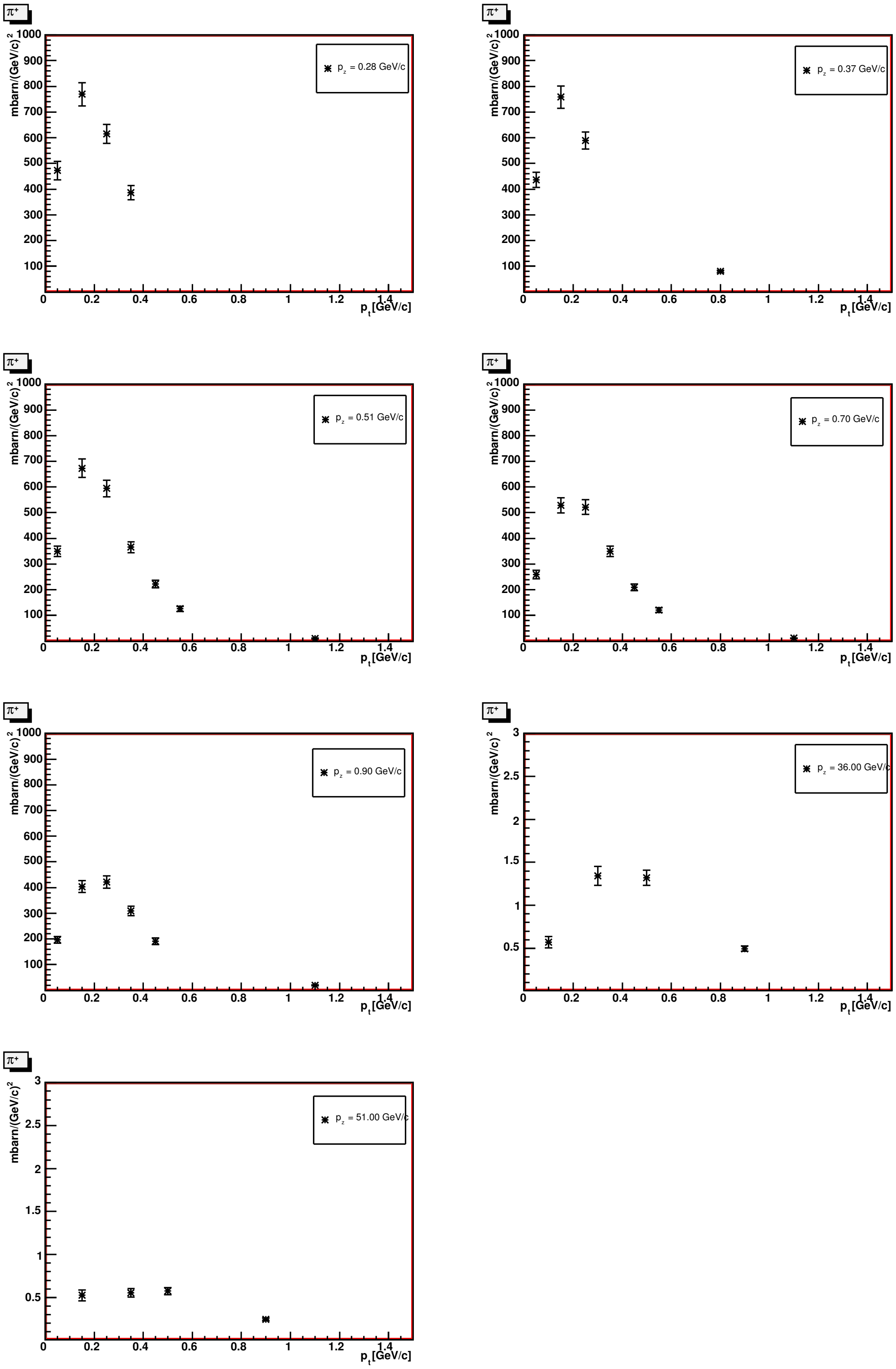

Figure 6.1: Double differential cross sections for positive pions.

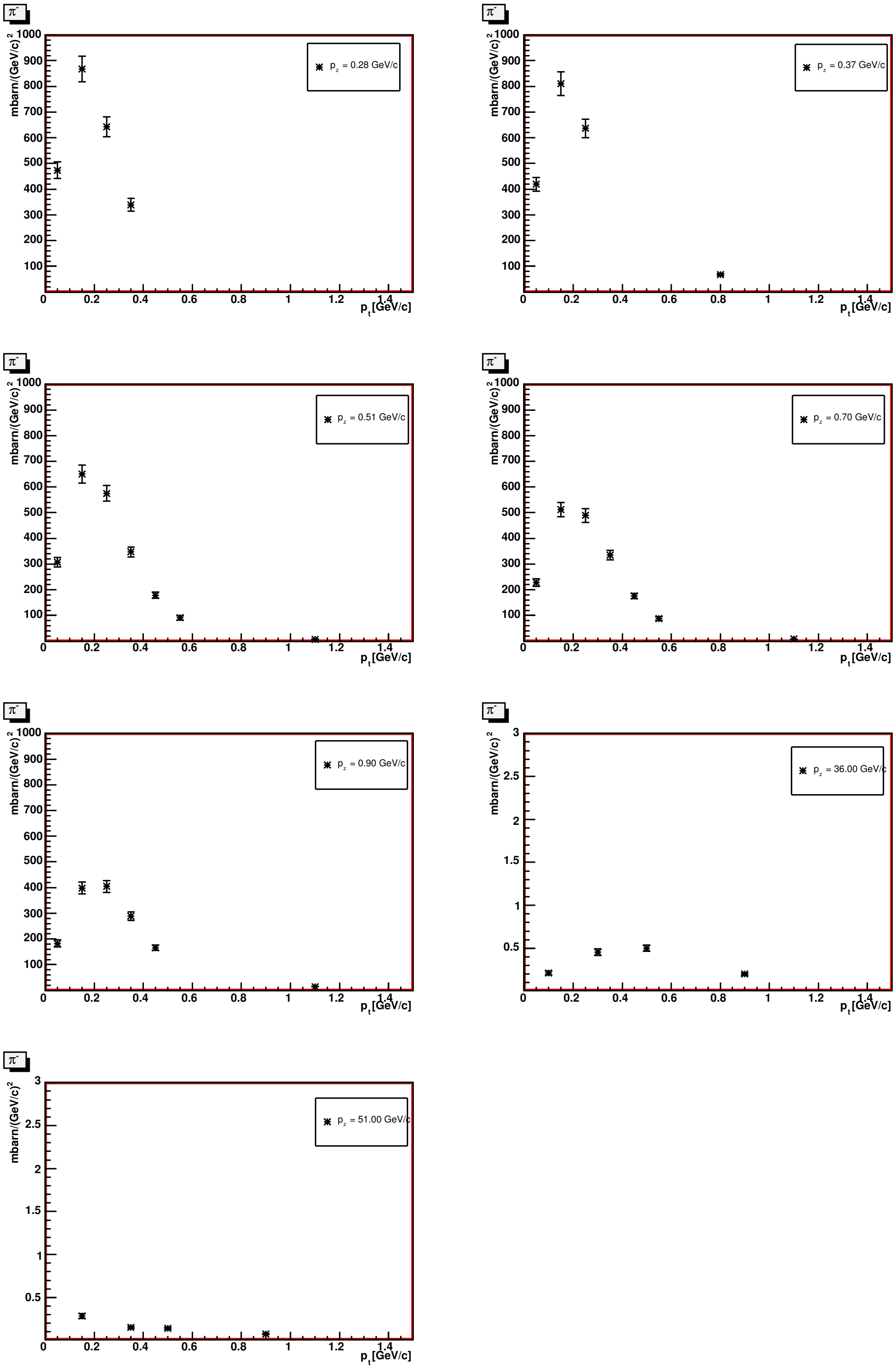

Figure 6.2: Double differential cross sections for negative pions.

Table 6.1: Cross section values and errors $p+C \rightarrow \pi^{+}+X$

Bin	p_z	p_t	$\frac{d^2\sigma_{\pi^+}}{dp_z dp_t}$	Erros in Percentage						
				Statistical	Total Systematics	Trigger Efficiency	vertex Z cut	Target out subtraction	Purity Correction	PID Efficiency
(0, 0)	0.28	0.05	$472.806^{+36.023}_{-35.152}$	3.2	$^{+6.9}_{-6.7}$	$^{+0.9}_{-0.8}$	$^{+0.0}_{-0.4}$	$^{+0.6}_{-0.6}$	$^{+1.6}_{-1.7}$	$^{+4.3}_{-4.0}$
(0, 1)	0.28	0.15	$769.905^{+45.258}_{-45.023}$	2.3	$^{+5.4}_{-5.4}$	$^{+1.0}_{-0.8}$	$^{+0.3}_{-0.4}$	$^{+0.6}_{-0.6}$	$^{+0.9}_{-0.9}$	$^{+1.5}_{-1.4}$
(0, 2)	0.28	0.25	$615.033^{+36.155}_{-36.102}$	2.8	$^{+5.2}_{-5.2}$	$^{+1.1}_{-0.9}$	$^{+0.2}_{-0.6}$	$^{+0.6}_{-0.6}$	$^{+0.3}_{-0.3}$	$^{+0.1}_{-0.1}$
(0, 3)	0.28	0.35	$387.123^{+27.353}_{-27.263}$	4.7	$^{+5.3}_{-5.3}$	$^{+1.2}_{-1.0}$	$^{+0.3}_{-0.5}$	$^{+0.6}_{-0.7}$	$^{+0.6}_{-0.6}$	$^{+0.8}_{-0.8}$
(1, 0)	0.37	0.05	$436.310^{+28.834}_{-28.594}$	2.9	$^{+5.9}_{-5.9}$	$^{+0.9}_{-0.7}$	$^{+0.1}_{-0.4}$	$^{+0.6}_{-0.6}$	$^{+1.2}_{-1.3}$	$^{+2.7}_{-2.6}$
(1, 1)	0.37	0.15	$758.127^{+43.646}_{-43.490}$	2.0	$^{+5.4}_{-5.4}$	$^{+0.9}_{-0.8}$	$^{+0.1}_{-0.4}$	$^{+0.6}_{-0.7}$	$^{+0.6}_{-0.6}$	$^{+1.5}_{-1.5}$
(1, 2)	0.37	0.25	$589.918^{+33.474}_{-33.457}$	2.3	$^{+5.2}_{-5.2}$	$^{+1.0}_{-0.9}$	$^{+0.1}_{-0.6}$	$^{+0.6}_{-0.6}$	$^{+0.3}_{-0.3}$	$^{+0.6}_{-0.6}$
(1, 3)	0.37	0.80	$79.702^{+4.823}_{-4.799}$	3.0	$^{+5.3}_{-5.2}$	$^{+1.3}_{-1.0}$	$^{+0.3}_{-0.4}$	$^{+0.6}_{-0.6}$	$^{+0.6}_{-0.6}$	$^{+0.4}_{-0.4}$
(2, 0)	0.51	0.05	$349.818^{+20.941}_{-20.789}$	2.4	$^{+5.5}_{-5.4}$	$^{+0.9}_{-0.8}$	$^{+0.7}_{-0.6}$	$^{+0.6}_{-0.6}$	$^{+1.0}_{-1.0}$	$^{+1.6}_{-1.5}$
(2, 1)	0.51	0.15	$673.227^{+36.571}_{-36.451}$	1.6	$^{+5.2}_{-5.2}$	$^{+0.9}_{-0.7}$	$^{+0.2}_{-0.3}$	$^{+0.6}_{-0.6}$	$^{+0.5}_{-0.5}$	$^{+0.7}_{-0.7}$
(2, 2)	0.51	0.25	$594.062^{+32.102}_{-32.003}$	1.7	$^{+5.1}_{-5.1}$	$^{+1.0}_{-0.8}$	$^{+0.1}_{-0.4}$	$^{+0.6}_{-0.6}$	$^{+0.2}_{-0.2}$	$^{+0.3}_{-0.3}$
(2, 3)	0.51	0.35	$365.678^{+20.747}_{-20.650}$	2.3	$^{+5.2}_{-5.1}$	$^{+1.1}_{-0.9}$	$^{+0.1}_{-0.3}$	$^{+0.6}_{-0.6}$	$^{+0.3}_{-0.3}$	$^{+0.1}_{-0.1}$
(2, 4)	0.51	0.45	$222.610^{+14.383}_{-14.316}$	3.7	$^{+5.3}_{-5.2}$	$^{+1.3}_{-1.1}$	$^{+0.2}_{-0.3}$	$^{+0.6}_{-0.6}$	$^{+0.7}_{-0.7}$	$^{+0.6}_{-0.6}$
(2, 5)	0.51	0.55	$125.751^{+10.753}_{-10.710}$	6.4	$^{+5.6}_{-5.6}$	$^{+1.3}_{-1.1}$	$^{+0.3}_{-0.3}$	$^{+0.6}_{-0.6}$	$^{+1.2}_{-1.2}$	$^{+1.7}_{-1.7}$
(2, 6)	0.51	1.10	$10.515^{+1.196}_{-1.194}$	10.0	$^{+5.5}_{-5.5}$	$^{+1.3}_{-1.1}$	$^{+0.3}_{-0.4}$	$^{+0.7}_{-0.7}$	$^{+1.1}_{-1.1}$	$^{+1.4}_{-1.3}$
(3, 0)	0.70	0.05	$259.361^{+16.192}_{-16.296}$	3.2	$^{+5.3}_{-5.4}$	$^{+0.8}_{-0.7}$	$^{+0.6}_{-1.0}$	$^{+0.5}_{-0.5}$	$^{+1.4}_{-1.5}$	$^{+0.3}_{-0.3}$
(3, 1)	0.70	0.15	$528.676^{+29.677}_{-29.674}$	1.8	$^{+5.3}_{-5.3}$	$^{+0.8}_{-0.7}$	$^{+0.1}_{-0.5}$	$^{+0.6}_{-0.6}$	$^{+1.0}_{-1.0}$	$^{+1.1}_{-1.0}$
(3, 2)	0.70	0.25	$521.937^{+28.340}_{-28.242}$	1.8	$^{+5.1}_{-5.1}$	$^{+1.0}_{-0.8}$	$^{+0.1}_{-0.3}$	$^{+0.6}_{-0.6}$	$^{+0.3}_{-0.3}$	$^{+0.0}_{-0.0}$

Table 6.1 continued

Bin	p_z	p_t	$\frac{d^2\sigma_{\pi^+}}{dp_z dp_t}$	Erros in Percentage						
				Statistical	Total Systematics	Trigger Efficiency	vertex Z cut	Target out subtraction	Purity Correction	PID Efficiency
(3, 3)	0.70	0.35	$349.648^{+19.662}_{-19.596}$	2.3	+5.1 −5.1	+1.0 −0.9	+0.2 −0.4	+0.6 −0.6	+0.1 −0.1	+0.2 −0.2
(3, 4)	0.70	0.45	$209.948^{+12.946}_{-12.879}$	3.3	+5.2 −5.2	+1.2 −1.0	+0.2 −0.3	+0.6 −0.6	+0.7 −0.7	+0.1 −0.1
(3, 5)	0.70	0.55	$121.299^{+9.456}_{-9.432}$	5.6	+5.5 −5.4	+1.3 −1.1	+0.2 −0.3	+0.6 −0.6	+1.5 −1.6	+0.5 −0.5
(3, 6)	0.70	1.10	$11.997^{+1.103}_{-1.101}$	7.3	+5.6 −5.5	+1.3 −1.1	+0.2 −0.4	+0.6 −0.6	+1.6 −1.7	+1.1 −1.1
(4, 0)	0.90	0.05	$196.166^{+13.259}_{-13.217}$	3.9	+5.5 −5.5	+0.8 −0.7	+0.5 −0.6	+0.6 −0.6	+1.1 −1.1	+1.8 −1.7
(4, 1)	0.90	0.15	$403.704^{+22.818}_{-22.801}$	2.1	+5.2 −5.2	+0.9 −0.7	+0.2 −0.4	+0.6 −0.6	+1.1 −1.1	+0.2 −0.2
(4, 2)	0.90	0.25	$422.234^{+23.733}_{-23.587}$	2.1	+5.2 −5.2	+0.9 −0.8	+0.5 −0.3	+0.6 −0.6	+0.4 −0.4	+0.9 −0.9
(4, 3)	0.90	0.35	$309.476^{+18.241}_{-18.145}$	2.5	+5.3 −5.3	+1.0 −0.9	+0.3 −0.3	+0.6 −0.6	+0.1 −0.1	+1.3 −1.3
(4, 4)	0.90	0.45	$190.639^{+13.142}_{-12.999}$	3.7	+5.8 −5.7	+1.2 −1.0	+0.2 −0.2	+0.6 −0.6	+0.5 −0.5	+2.6 −2.4
(4, 5)	0.90	1.10	$19.675^{+1.421}_{-1.408}$	4.1	+6.0 −5.9	+1.3 −1.1	+0.1 −0.3	+0.6 −0.6	+1.3 −1.3	+2.6 −2.5
(5, 0)	36.00	0.10	$0.571^{+0.068}_{-0.058}$	4.4	+11.0 −9.1	+2.9 −2.5	+5.3 −2.3	+0.7 −0.7	+2.0 −2.0	+7.4 −6.5
(5, 1)	36.00	0.30	$1.342^{+0.111}_{-0.105}$	2.8	+7.8 −7.3	+2.5 −2.2	+3.0 −2.4	+0.6 −0.6	+1.1 −1.1	+4.4 −4.0
(5, 2)	36.00	0.50	$1.321^{+0.089}_{-0.085}$	2.8	+6.1 −5.8	+2.3 −2.0	+2.3 −1.7	+0.7 −0.7	+1.2 −1.2	+0.2 −0.2
(5, 3)	36.00	0.90	$0.495^{+0.031}_{-0.030}$	2.6	+5.7 −5.4	+2.0 −1.7	+1.5 −1.0	+0.6 −0.6	+0.7 −0.7	+0.0 −0.0
(6, 0)	51.00	0.15	$0.524^{+0.064}_{-0.053}$	4.4	+11.3 −9.1	+2.7 −2.3	+5.8 −2.7	+0.7 −0.7	+1.2 −1.2	+7.7 −6.6
(6, 1)	51.00	0.35	$0.553^{+0.049}_{-0.047}$	5.6	+6.9 −6.4	+2.8 −2.4	+3.6 −2.7	+0.7 −0.8	+0.8 −0.8	+1.2 −1.1
(6, 2)	51.00	0.50	$0.574^{+0.041}_{-0.040}$	3.7	+6.2 −5.9	+2.6 −2.3	+2.4 −1.9	+0.6 −0.6	+0.8 −0.8	+0.0 −0.0
(6, 3)	51.00	0.90	$0.247^{+0.017}_{-0.016}$	3.4	+5.8 −5.7	+2.3 −2.0	+1.4 −1.6	+0.6 −0.7	+0.6 −0.6	+0.1 −0.1

Table 6.2: Cross section values and errors p+$C \rightarrow \pi^-$+X

Bin	p_z	p_t	$\frac{d^2\sigma_{\pi^-}}{dp_z dp_t}$	Erros in Percentage						
				Statistical	Total Systematics	Trigger Efficiency	vertex Z cut	Target out subtraction	Purity Correction	PID Efficiency
(0, 0)	0.28	0.05	$474.114^{+32.978}_{-33.023}$	3.2	$^{+6.2}_{-6.2}$	$^{+0.8}_{-0.7}$	$^{+0.3}_{-0.4}$	$^{+0.5}_{-0.5}$	$^{+2.5}_{-2.7}$	$^{+2.3}_{-2.2}$
(0, 1)	0.28	0.15	$866.985^{+49.947}_{-49.623}$	2.3	$^{+5.3}_{-5.3}$	$^{+0.9}_{-0.8}$	$^{+0.5}_{-0.3}$	$^{+0.6}_{-0.6}$	$^{+0.8}_{-0.8}$	$^{+1.0}_{-1.0}$
(0, 2)	0.28	0.25	$642.944^{+37.957}_{-37.783}$	2.8	$^{+5.2}_{-5.2}$	$^{+1.2}_{-1.0}$	$^{+0.2}_{-0.4}$	$^{+0.6}_{-0.6}$	$^{+0.3}_{-0.3}$	$^{+0.5}_{-0.5}$
(0, 3)	0.28	0.35	$339.265^{+25.198}_{-24.983}$	4.7	$^{+5.8}_{-5.7}$	$^{+1.2}_{-1.0}$	$^{+0.2}_{-0.3}$	$^{+0.6}_{-0.6}$	$^{+0.2}_{-0.2}$	$^{+2.5}_{-2.4}$
(1, 0)	0.37	0.05	$419.391^{+26.554}_{-26.622}$	2.9	$^{+5.6}_{-5.6}$	$^{+0.8}_{-0.6}$	$^{+0.3}_{-0.5}$	$^{+0.5}_{-0.5}$	$^{+2.0}_{-2.0}$	$^{+1.3}_{-1.3}$
(1, 1)	0.37	0.15	$811.195^{+46.000}_{-45.855}$	2.0	$^{+5.3}_{-5.3}$	$^{+0.9}_{-0.7}$	$^{+0.2}_{-0.3}$	$^{+0.6}_{-0.6}$	$^{+0.7}_{-0.8}$	$^{+1.1}_{-1.1}$
(1, 2)	0.37	0.25	$637.225^{+36.003}_{-35.834}$	2.3	$^{+5.2}_{-5.1}$	$^{+1.1}_{-0.9}$	$^{+0.1}_{-0.2}$	$^{+0.6}_{-0.6}$	$^{+0.2}_{-0.2}$	$^{+0.3}_{-0.3}$
(1, 3)	0.37	0.80	$67.674^{+4.226}_{-4.194}$	3.0	$^{+5.5}_{-5.4}$	$^{+1.2}_{-1.0}$	$^{+0.1}_{-0.3}$	$^{+0.6}_{-0.6}$	$^{+0.3}_{-0.3}$	$^{+1.7}_{-1.7}$
(2, 0)	0.51	0.05	$307.587^{+17.995}_{-17.935}$	2.4	$^{+5.3}_{-5.3}$	$^{+0.8}_{-0.7}$	$^{+0.5}_{-0.5}$	$^{+0.5}_{-0.5}$	$^{+1.2}_{-1.2}$	$^{+0.8}_{-0.8}$
(2, 1)	0.51	0.15	$650.730^{+35.002}_{-34.957}$	1.6	$^{+5.1}_{-5.1}$	$^{+0.9}_{-0.7}$	$^{+0.2}_{-0.4}$	$^{+0.6}_{-0.6}$	$^{+0.4}_{-0.4}$	$^{+0.2}_{-0.2}$
(2, 2)	0.51	0.25	$575.281^{+31.007}_{-30.883}$	1.7	$^{+5.1}_{-5.1}$	$^{+0.9}_{-0.8}$	$^{+0.1}_{-0.2}$	$^{+0.6}_{-0.6}$	$^{+0.1}_{-0.1}$	$^{+0.2}_{-0.2}$
(2, 3)	0.51	0.35	$347.087^{+19.597}_{-19.524}$	2.3	$^{+5.1}_{-5.1}$	$^{+1.0}_{-0.9}$	$^{+0.1}_{-0.3}$	$^{+0.6}_{-0.6}$	$^{+0.1}_{-0.1}$	$^{+0.0}_{-0.0}$
(2, 4)	0.51	0.45	$179.194^{+12.256}_{-12.134}$	3.7	$^{+5.7}_{-5.6}$	$^{+1.2}_{-1.0}$	$^{+0.2}_{-0.2}$	$^{+0.6}_{-0.6}$	$^{+0.2}_{-0.2}$	$^{+2.5}_{-2.3}$
(2, 5)	0.51	0.55	$91.519^{+8.270}_{-8.164}$	6.4	$^{+6.3}_{-6.2}$	$^{+1.2}_{-1.0}$	$^{+0.1}_{-0.3}$	$^{+0.6}_{-0.6}$	$^{+0.2}_{-0.2}$	$^{+3.6}_{-3.4}$
(2, 6)	0.51	1.10	$7.585^{+0.871}_{-0.868}$	10.0	$^{+5.7}_{-5.7}$	$^{+1.2}_{-1.0}$	$^{+0.1}_{-0.4}$	$^{+0.6}_{-0.6}$	$^{+0.2}_{-0.2}$	$^{+2.4}_{-2.3}$
(3, 0)	0.70	0.05	$227.712^{+15.299}_{-15.228}$	3.2	$^{+5.9}_{-5.8}$	$^{+0.9}_{-0.8}$	$^{+0.9}_{-1.2}$	$^{+0.6}_{-0.6}$	$^{+0.3}_{-0.3}$	$^{+2.7}_{-2.6}$
(3, 1)	0.70	0.15	$512.328^{+27.800}_{-27.852}$	1.8	$^{+5.1}_{-5.1}$	$^{+0.8}_{-0.7}$	$^{+0.2}_{-0.6}$	$^{+0.6}_{-0.6}$	$^{+0.2}_{-0.2}$	$^{+0.2}_{-0.2}$
(3, 2)	0.70	0.25	$489.485^{+26.474}_{-26.430}$	1.8	$^{+5.1}_{-5.1}$	$^{+0.8}_{-0.7}$	$^{+0.2}_{-0.4}$	$^{+0.6}_{-0.6}$	$^{+0.1}_{-0.1}$	$^{+0.2}_{-0.2}$
(3, 3)	0.70	0.35	$335.434^{+18.782}_{-18.753}$	2.3	$^{+5.1}_{-5.1}$	$^{+0.9}_{-0.8}$	$^{+-0.0}_{-0.4}$	$^{+0.6}_{-0.6}$	$^{+0.1}_{-0.1}$	$^{+0.2}_{-0.2}$

Table 6.2 continued

Bin	p_z	p_t	$\frac{d^2\sigma_{\pi^-}}{dp_z dp_t}$	Erros in Percentage						
				Statistical	Total Systematics	Trigger Efficiency	vertex Z cut	Target out subtraction	Purity Correction	PID Efficiency
(3, 4)	0.70	0.45	$175.699^{+10.699}_{-10.666}$	3.3	$^{+5.1}_{-5.1}$	$^{+1.0}_{-0.9}$	$^{+0.2}_{-0.3}$	$^{+0.6}_{-0.6}$	$^{+0.1}_{-0.1}$	$^{+0.1}_{-0.1}$
(3, 5)	0.70	0.55	$88.271^{+6.905}_{-6.873}$	5.6	$^{+5.5}_{-5.4}$	$^{+1.1}_{-0.9}$	$^{+0.2}_{-0.3}$	$^{+0.6}_{-0.6}$	$^{+0.2}_{-0.2}$	$^{+1.9}_{-1.8}$
(3, 6)	0.70	1.10	$8.296^{+0.745}_{-0.743}$	7.3	$^{+5.2}_{-5.2}$	$^{+1.2}_{-1.0}$	$^{+0.2}_{-0.4}$	$^{+0.6}_{-0.6}$	$^{+0.2}_{-0.2}$	$^{+0.4}_{-0.4}$
(4, 0)	0.90	0.05	$182.733^{+14.084}_{-13.809}$	3.9	$^{+6.6}_{-6.5}$	$^{+0.9}_{-0.7}$	$^{+0.8}_{-1.1}$	$^{+0.5}_{-0.5}$	$^{+0.4}_{-0.4}$	$^{+4.2}_{-3.8}$
(4, 1)	0.90	0.15	$398.304^{+22.539}_{-22.579}$	2.1	$^{+5.2}_{-5.2}$	$^{+0.8}_{-0.6}$	$^{+0.3}_{-0.7}$	$^{+0.6}_{-0.6}$	$^{+0.1}_{-0.1}$	$^{+1.2}_{-1.2}$
(4, 2)	0.90	0.25	$404.862^{+22.869}_{-22.775}$	2.1	$^{+5.3}_{-5.2}$	$^{+0.8}_{-0.7}$	$^{+0.1}_{-0.2}$	$^{+0.6}_{-0.6}$	$^{+0.1}_{-0.1}$	$^{+1.3}_{-1.3}$
(4, 3)	0.90	0.35	$288.344^{+16.711}_{-16.688}$	2.5	$^{+5.2}_{-5.2}$	$^{+0.9}_{-0.8}$	$^{+0.0}_{-0.4}$	$^{+0.6}_{-0.6}$	$^{+0.1}_{-0.1}$	$^{+1.0}_{-1.0}$
(4, 4)	0.90	0.45	$166.265^{+10.750}_{-10.713}$	3.7	$^{+5.3}_{-5.2}$	$^{+1.0}_{-0.9}$	$^{+0.2}_{-0.3}$	$^{+0.6}_{-0.6}$	$^{+0.1}_{-0.1}$	$^{+1.2}_{-1.2}$
(4, 5)	0.90	1.10	$14.893^{+1.038}_{-1.030}$	4.1	$^{+5.7}_{-5.6}$	$^{+1.1}_{-0.9}$	$^{+0.2}_{-0.4}$	$^{+0.6}_{-0.6}$	$^{+0.2}_{-0.2}$	$^{+2.3}_{-2.2}$
(5, 0)	36.00	0.10	$0.211^{+0.023}_{-0.020}$	4.4	$^{+10.0}_{-8.6}$	$^{+2.7}_{-2.3}$	$^{+5.7}_{-3.7}$	$^{+0.6}_{-0.6}$	$^{+1.8}_{-1.9}$	$^{+5.6}_{-5.0}$
(5, 1)	36.00	0.30	$0.455^{+0.038}_{-0.036}$	2.8	$^{+7.8}_{-7.3}$	$^{+2.4}_{-2.1}$	$^{+2.6}_{-2.0}$	$^{+0.6}_{-0.6}$	$^{+1.5}_{-1.6}$	$^{+4.6}_{-4.2}$
(5, 2)	36.00	0.50	$0.501^{+0.036}_{-0.032}$	2.8	$^{+6.6}_{-5.8}$	$^{+2.4}_{-2.0}$	$^{+3.3}_{-1.6}$	$^{+0.6}_{-0.6}$	$^{+1.2}_{-1.3}$	$^{+0.1}_{-0.1}$
(5, 3)	36.00	0.90	$0.199^{+0.013}_{-0.012}$	2.6	$^{+5.8}_{-5.6}$	$^{+1.9}_{-1.6}$	$^{+2.0}_{-1.7}$	$^{+0.6}_{-0.6}$	$^{+0.8}_{-0.8}$	$^{+0.0}_{-0.0}$
(6, 0)	51.00	0.15	$0.283^{+0.029}_{-0.027}$	4.4	$^{+9.3}_{-8.5}$	$^{+2.1}_{-1.8}$	$^{+2.6}_{-2.1}$	$^{+0.6}_{-0.6}$	$^{+1.0}_{-1.0}$	$^{+7.0}_{-6.2}$
(6, 1)	51.00	0.35	$0.151^{+0.013}_{-0.013}$	5.6	$^{+6.2}_{-6.2}$	$^{+2.5}_{-2.1}$	$^{+1.1}_{-1.7}$	$^{+0.5}_{-0.5}$	$^{+0.9}_{-0.9}$	$^{+2.1}_{-2.0}$
(6, 2)	51.00	0.50	$0.141^{+0.010}_{-0.010}$	3.7	$^{+6.3}_{-5.8}$	$^{+2.7}_{-2.3}$	$^{+2.4}_{-1.3}$	$^{+0.7}_{-0.7}$	$^{+0.9}_{-1.0}$	$^{+0.2}_{-0.2}$
(6, 3)	51.00	0.90	$0.073^{+0.005}_{-0.005}$	3.4	$^{+5.6}_{-5.5}$	$^{+2.2}_{-1.8}$	$^{+1.1}_{-1.2}$	$^{+0.6}_{-0.6}$	$^{+0.7}_{-0.8}$	$^{+0.1}_{-0.1}$

REFERENCES

[1] J. Ranft A. Fasso, A. Ferrari and P.R. Sala. Fluka: a multi-particle transport code. *CERN 2005-10, INFN/TC-05/11, SLAC-R-773*, 2005.

[2] Minerva Collaboration. *The Minerva technical design report*, 2006.

[3] MINOS Collaboration. *The MINOS technical design report*, 1998.

[4] MIPP Collaboration. *The MIPP Trigger Document.*

[5] MIPP Collaboration. *P-907: Proposal to Measure Particle Production in the Meson Area Using Main Injector Primary and Secondary Beams.*

[6] NuMI Collaboration. *NuMI Technical Design Handbook*, 2004.

[7] SPY Collaboration. Measurement of charged particle production from 450 gev/c protons on beryllium. *Eur. Phys. J. C*, 10(605), 1999.

[8] D.S. Barton et al. Experimental study of the a-dependence of inclusive hadron fragmentation. *Phys. Rev. D*, 27(2580-2589), 1983.

[9] G. Rai et al. A tpc detector for the study of high multiplicity heavy ion collisions. *IEEE Trans. Nucl. Sc*, 37(56-64), 1990.

[10] H.W. Atherton et al. Precise measurements of particle production by 400-gev/c protons on beryllium targets. *CERN-80-07.*, 1980.

[11] K.L. Lee et al. Analog-to-digital conversion using custom cmos analog memory for the eos time projection chambers. *IEEE Trans. Nucl. Sc*, 38(344-347), 1991.

[12] M. De Palma et al. A system of large multiwire proportional chambers for a high intensity experiment. *Nuclear Instrument Methods*, 217(135), 1983.

[13] R.A. Burnstein et al [HyperCP]. A high-rate spectrometer for the study of charged hyperon and kaon decays. *Nucl. Instrum. Meth*, A541(516-565), 2005.

[14] Ron Jones Fred Bieser and Charles McParland. Data links for the eos tpc. *IEEE Trans. Nucl. Sc*, 38(335-336), 1991.

[15] Ed Hartouni. First order memory dump on the e766/e690/e910/e895/e907 threshold cerenkov counter. 2002.

[16] P.D. Barnes M. Heffner J. Klay J. Paley, R.Soltz and D.Miller. *MIPP TPC reconstruction*, 2006. MIPP Note, 129.

[17] J.C.Tarle H.Verveij J.B. Lindsay, C.Millerin and H. Wendler. A fast and flexible data acquisition system for multiwire proportional chambers and other detectors. *Nuclear Instrument Methods*, 156(329-333), 1978.

[18] Nicholas J.Graf. *Measurement of the Charged Kaon Mass with the MIPP RICH*. PhD thesis, July 2008.

[19] A. Lebedev. *Ratio of Pion Kaon Production in Proton Carbon Interaction*. PhD thesis, Harvard University, May 2007.

[20] D.A. Landis M. Nakamura and G. Rai. Low power shaper amplifier for the eos tpc detector. *IEEE Trans. Nucl. Sc*, 38(50-52), 1991.

[21] R.Raja M.Albrow. *Hadronic Shower Simulation Workshop*, volume 896. AIP Conference Proceedings, May 2007.

[22] Holger Meyer. *How to get Cross Sections from MIPP data*, 2009. MIPP-doc-871-v2.

[23] N. Mokhov. Mars code system. available at `http://www-ap.fnal.gov/MARS/`.

[24] Rajendran Raja. Observation of a new regularity in hadronic spectra. *Physical Review D*, 18(1), 1978.

[25] S. M. Seun. *Measurement of* $\pi - K$ *Ratios from NuMI Target*. PhD thesis, Harvard University, July 2007.